Journal of Applied Physics

RESEARCH ARTICLE | SEPTEMBER 05 2023

Coherence effects on the interference colors of soap films

Navraj S. Lalli ; Andrea Giusti

J. Appl. Phys. 134, 093103 (2023)
https://doi.org/10.1063/5.0158178

Journal of Applied Physics ARTICLE pubs.aip.org/aip/jap

Coherence effects on the interference colors of soap films

Cite as: J. Appl. Phys. **134**, 093103 (2023); doi: 10.1063/5.0158178
Submitted: 15 May 2023 · Accepted: 7 August 2023 ·
Published Online: 5 September 2023

Navraj S. Lalli[a] and Andrea Giusti

AFFILIATIONS

Department of Mechanical Engineering, Imperial College London, South Kensington Campus, London SW7 2AZ, United Kingdom

[a]**Author to whom correspondence should be addressed:** nsl16@ic.ac.uk

ABSTRACT

Acquiring the thickness field of a soap film from interference colors requires an accurate relationship between color and film thickness. Throughout the literature, an interference relation derived using monochromatic waves is widely used to calculate the colors of soap films illuminated by light sources with significant frequency bandwidths by applying the relation at a number of discrete wavelengths in the source, which assumes that the interfering waves are perfectly coherent. However, since the coherence between waves is expected to decrease with increasing film thickness, it is poorly understood when interference relations derived using monochromatic waves can be applied. In this study, an interference relation incorporating the coherence between interfering waves is derived. The effects of coherence on the interference colors of soap films are then studied by comparing the colors computed using each of these two interference relations for light sources with different frequency bandwidths. As the frequency bandwidth of the light source increases, the difference in the colors computed using each interference relation increases, which implies that the accuracy of the method involving the monochromatic relation decreases with increasing frequency bandwidth of the source. The findings of this study will allow for more accurate measurements of the thickness of soap films from their interference colors.

I. INTRODUCTION

Soap films are thin layers of liquid stabilized by surfactant-laden interfaces. They typically have thicknesses between 4 nm and 10 μm.[1,2] Soap films with spatial variations in their thickness exhibit colorful interference fringes when they are illuminated. Experiments involving soap films have exploited the visual nature of these interference fringes to advance several fields of research. For example, soap films have been used to investigate forced and decaying two-dimensional turbulence, revealing key differences in the turbulent spectra between two and three-dimensional turbulent flows.[3,4] Meuel *et al.*[5] used interference fringes to study large vortices on soap bubbles, created by heating half of each bubble from below. Their analysis suggests that there may be features in common between the two-dimensional vortices that they observed on soap films and three-dimensional tropical cyclones, which could lead to the use of soap films to study vortices in a range of three-dimensional turbulent flows. Soap films can also be used to investigate the flows created when a fluid interacts with a solid, such as the flow generated by flapping wings[6] or the flow in the wake of a solid object.[7,8]

The thickness of a soap film not only provides useful information about the fluid mechanics of the film but is also of fundamental importance to the film stability: thinner soap films are less stable and therefore more likely to burst than thicker films.[9] When a soap film is formed, it starts thinning through drainage and evaporation. The time evolution of the thickness field of a soap film provides insight into the film stability and allows drainage mechanisms, such as marginal regeneration,[10,11] to be investigated. Thickness measurements from experiments can also be used to validate models for the thinning of films.[12] With a further understanding of the thinning mechanisms taking place in soap films, new methods can be developed to control film thinning and film stability. The ability to control film stability could lead to the development of novel applications, such as the use of bubbles as smart carriers for the targeted release of a substance transported by the bubble. Recent work featuring the application of a magnetic field to soap films containing magnetic nanoparticles provides evidence that an external field can be used to control film stability.[13] The development of an accurate method to obtain the thickness field of a soap film over time is a prerequisite to drive these innovations.

Since the temporal evolution of film thickness is desired, invasive methods, such as contact profilometry[14] and capacitance methods,[15] are unsuitable as they disrupt the drainage in the film and may induce film rupture. Widely used non-invasive techniques for measuring the film thickness of soap films include phase-shifting interferometry,[16,17] scanning interferometry,[18] laser reflectometry,[19–21] spectroscopic reflectometry,[22] infrared absorption,[23] and absorption spectroscopy.[24,25] Although these methods can result in accurate film thickness measurements, they can typically only make a single film thickness measurement at a time, which makes them unsuitable for measuring thickness fields at a given time instant. However, the spatiotemporal evolution of film thickness can be found through a simple experimental setup featuring a light source and a camera, as depicted in Fig. 1(a). The thickness evolution can be found by recording the colors arising from light interference and mapping the colors to thickness, which requires an accurate relationship between thickness and color. Figure 1(b) provides an example of interference colors exhibited by an illuminated soap film recorded with this experimental setup.

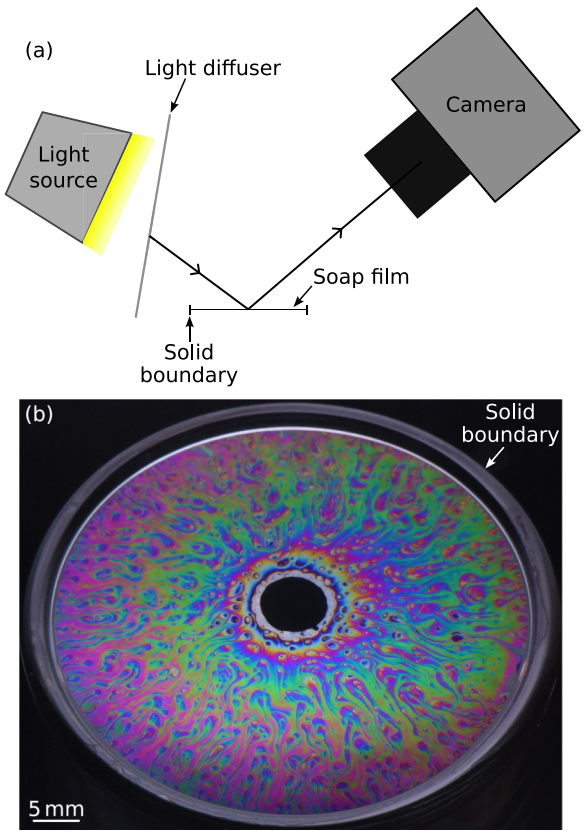

FIG. 1. (a) A simple experimental setup for measuring the thickness field of a soap film and (b) interference colors exhibited by a soap film recorded with this setup.

In the soap film literature, interference calculations are widely performed using interference relations derived for monochromatic waves created from a single incident light wave by amplitude division.[26–34] These interference relations are largely similar but with some differences. For instance, Dias accounts for different materials on either side of the film[27,28] and Jaszkowski and Rzeszut extend the usually adopted scenario of two interfering waves to any number of interfering waves.[32] These interference relations are commonly used to find the thickness–color relationship for soap films illuminated by white light by applying the relation at a discrete number of wavelengths in the source, as detailed in Refs. 29–33. This method is also implemented in the open-source Python package ColorPy.[35] Since monochromatic waves have an infinite coherence length, it is implicit in this method that the interfering waves are perfectly coherent, regardless of the film thickness. Interference is then predicted to occur for any film thickness. In reality, the coherence between interfering waves leaving one of the surfaces of a soap film falls as the film thickness increases because real light sources (light sources with a non-zero frequency bandwidth) have a finite coherence length.[36] This reduces the amount of interference occurring and is one of the key reasons why interference phenomena are not observed for sufficiently thick soap films illuminated by white light. Consequently, it is largely unclear when interference relations derived using monochromatic waves can be used for real light sources and over what range of film thicknesses.

The objectives of this work are then to (i) derive an interference relation that accounts for the coherence between interfering waves and (ii) to provide insight over what range of film thicknesses and light source bandwidths interference relations derived using monochromatic waves can accurately calculate interference colors. To achieve these objectives, an interference relation for monochromatic waves will first be re-derived and generalized with the intention of highlighting all key assumptions and physics that often go unstated. Then, a relation that accounts for coherence effects will be introduced. The generalized relation for monochromatic waves and the newly introduced relation accounting for coherence effects will then be applied to find the variation of color with film thickness for light sources of different frequency bandwidths.

The remainder of this paper is organized as follows. First, the derivations of the interference relation for monochromatic waves and the interference relation accounting for coherence effects are discussed. Then, the method for converting a spectral irradiance distribution to color is detailed. Following this, the interference colors computed using each of the two interference relations are analyzed. Conclusions close the paper.

II. SPECTRAL DISTRIBUTION OF LIGHT AT A DETECTOR

This section provides a detailed derivation of the interference relation for monochromatic waves and the interference relation incorporating the effects of coherence. Before presenting the derivations, which are given in Secs. II H and II I, the fundamentals of classical optics in the context of an illuminated soap film are detailed to introduce the required concepts and notation.

A. Classical description of light

Light is emitted in discrete bursts commonly referred to as photons, and any observed light consists of an extremely large number of low-energy photons.[36] When averaging over time, the radiant energy delivered by an extremely large number of photons is the same as the energy delivered by a classical electromagnetic wave. As a result, light can be treated as a classical electromagnetic wave when performing interference calculations. The term "light wave" will frequently be used to refer to this classical electromagnetic wave, and the wavelength range for visible light is from 360 to 830 nm.[37]

Light waves oscillate at frequencies of the order of 1 THz; therefore, visible-light detectors cannot measure the instantaneous power delivered by light waves. Instead, the radiant energy entering through an area A in the detector is measured over a period of time Υ much larger than the time period of the electromagnetic wave. Similarly, since it not possible to filter single frequencies from the light source, the detector will measure the radiant energy in a small wavelength range. Dividing the measured radiant energy by the period Υ leads to the radiant flux and additionally dividing by the area A results in the radiant flux density in this wavelength range. Since this radiant energy is incident upon the detector surface, the radiant flux density may be referred to as the irradiance, I. Dividing the irradiance by the small wavelength range results in the spectral irradiance, I_λ, in units of $\mathrm{W\,m^{-2}\,nm^{-1}}$. A source of light is characterized by its spectral irradiance distribution, i.e., the variation of I_λ with the wavelength of light, λ. Although the irradiance at a specific wavelength λ_0 is undefined, the irradiance can be found in a wavelength interval, $\Delta\lambda$, centered at λ_0,

$$I(\lambda_0) = \int_{\lambda_0-\Delta\lambda/2}^{\lambda_0+\Delta\lambda/2} I_\lambda(\lambda)\,\mathrm{d}\lambda. \tag{1}$$

For small $\Delta\lambda$, $I(\lambda_0) \approx I_\lambda(\lambda_0)\Delta\lambda$.

The thickness–color relationship of any soap film depends on the spectral irradiance distribution of the light source used to illuminate the film. The overall process of converting from film thickness to color involves using the spectral irradiance distribution of the light source and considering light interference to find the spectral irradiance distribution measured by a detector for each film thickness. The detector could be the retina of the human eye or an electronic detector, such as a CCD or CMOS sensor.

In this study, the source of light and the detector will be in air. Introducing the electric field vector of the light wave as $\tilde{\boldsymbol{E}}$, the irradiance at a point in space in a linear, homogeneous, and isotropic dielectric, such as air, can be found from $\tilde{\boldsymbol{E}}$ by[36]

$$I = \epsilon_a v_a \langle \tilde{E}^2 \rangle_\Upsilon, \tag{2}$$

where ϵ_a is the electric permittivity of air, v_a is the velocity of light in air, and $\langle \tilde{E}^2 \rangle_\Upsilon$ is the time average of the magnitude of the electric field squared over a time period Υ.

B. Electric field representation

The electric field vector of a light wave can be represented, in general, by

$$\tilde{\boldsymbol{E}} = \boldsymbol{E}_0(\boldsymbol{r}, \tau)\cos\phi(\boldsymbol{r}, \tau), \tag{3}$$

where $\boldsymbol{E}_0$ is the amplitude of the electric field, ϕ is the phase of the electric field, $\boldsymbol{r}$ is the position vector with respect to an arbitrarily chosen origin, and τ is the time. For interference calculations, it is more convenient to work with a complex representation of the electric field,

$$\tilde{\boldsymbol{E}} = \Re\{\boldsymbol{E}\} = \Re\left\{\boldsymbol{E}_0(\boldsymbol{r}, \tau)\mathrm{e}^{\mathrm{i}\phi(\mathbf{r},\,\tau)}\right\}, \tag{4}$$

where $\boldsymbol{E}$ is the complex representation of the electric field vector, $\Re\{\boldsymbol{E}\}$ is the real part of $\boldsymbol{E}$, e is the base of the natural logarithm, and i is the unit imaginary number. The irradiance, given by Eq. (2), can be found from the complex representation using the result derived in Appendix A,

$$I = \frac{1}{2}\epsilon_a v_a \langle \boldsymbol{E}\cdot\boldsymbol{E}^* \rangle_\Upsilon, \tag{5}$$

where $\boldsymbol{E}^*$ is the complex conjugate of $\boldsymbol{E}$.

Since light of any polarization can be expressed as the sum of two linearly polarized waves that are polarized in orthogonal directions,[36] linearly polarized waves with constant polarization will be considered such that $\boldsymbol{E}_0(\boldsymbol{r}, \tau) = \boldsymbol{E}_0$.

In deriving a general interference relation that does not account for the coherence between interfering waves, the light wave from the light source will be treated as a linearly polarized monochromatic plane wave of wavelength λ_0, where λ_0 is the wavelength in air. The complex representation of the electric field vector of the light from the source, $\boldsymbol{E}_s$, is then

$$\boldsymbol{E}_s = \boldsymbol{E}_{0s}\mathrm{e}^{\mathrm{i}(\boldsymbol{k}_s\cdot\boldsymbol{r}-\omega_0\tau)}, \tag{6}$$

where $\boldsymbol{E}_{0s}$, $\boldsymbol{k}_s$, and ω_0 are the amplitude, wave vector, and angular frequency of this wave, respectively. The amplitude of $\boldsymbol{k}_s$ is $2\pi/\lambda_0$ and $\omega_0 = 2\pi v_a/\lambda_0$. No light wave is truly monochromatic because every light wave has a frequency bandwidth, even if very small. When treating the incident wave from the source as monochromatic, the interference colors can be calculated by assuming that each wavelength in the light source produces its own interference pattern and the overall interference pattern is the sum of the interference patterns due to each wavelength.[38]

When deriving the interference relation that accounts for the coherence between interfering waves, the monochromatic plane wave assumption will not be made.

C. Interference

Light interference involves the interaction of multiple electromagnetic waves and results in a wave with detected irradiance differing from the sum of the detected irradiances of each of the interacting waves. The electric field vector resulting from the interference of light waves at a detector, $\tilde{\boldsymbol{E}}_d$, is the sum of each electric

field interfering at the detector. The real and complex sums of the electric fields at the detector are

$$\tilde{\boldsymbol{E}}_{\mathrm{d}} = \sum_j \tilde{\boldsymbol{E}}_j \quad \text{and} \quad \boldsymbol{E}_{\mathrm{d}} = \sum_j \boldsymbol{E}_j. \tag{7}$$

Since $\tilde{\boldsymbol{E}}_{\mathrm{d}} = \Re\{\boldsymbol{E}_{\mathrm{d}}\}$, the detected irradiance, I_{d}, can be found by inserting $\boldsymbol{E}_{\mathrm{d}}$ in Eq. (5), i.e., $I_{\mathrm{d}} = \frac{1}{2}\epsilon_{\mathrm{a}} v_{\mathrm{a}} \langle \boldsymbol{E}_{\mathrm{d}} \cdot \boldsymbol{E}_{\mathrm{d}}^{*} \rangle_T$. Since the detected irradiance can be more easily found by only considering the complex representation, the real representation will not feature again in the present study.

D. Coherence

The coherence between light waves is of key importance to light interference, particularly since it is not usually accounted for when computing the thickness–color relationship of an illuminated soap film.[30–33]

Considering each photon as a wavetrain, a wavetrain occupies a fixed point in space over a period of time known as the coherence time, Δt_{c}, which is typically less than 10 ns.[36] For example, at each point in space illuminated by white light, the phase will vary predictably over a period of time given by the coherence time before the phase randomly shifts due to the arrival of another photon. The corresponding distance in space over which a wavetrain extends is known as the coherence length, Δl_{c}, and is given by $\Delta l_{\mathrm{c}} = v \Delta t_{\mathrm{c}}$, where v is the wave velocity. The coherence time is typically of the order of the inverse of the frequency bandwidth, Δf, of the light source ($\Delta t_{\mathrm{c}} \sim 1/\Delta f$), although this depends on the precise definitions used for Δt_{c} and Δf.[39]

The coherence between light waves refers to how correlated the waves are in space and time.[38] For multiple light waves to interfere, the waves must be at least partially coherent. When a light wave is emitted by two different points on an extended light source, the frequency bandwidth of the source determines whether the two light waves will interfere when they are focused onto a single point. For any real light source, the phase difference between the two waves will vary randomly in space and time due to the range of frequencies present in each light wave. Furthermore, any correlation will only exist for a time equal to the coherence time before randomly shifting. Therefore, as the frequency bandwidth of the light source is increased from a very small value, the correlation between the two waves would fall until no interference occurs. The two light waves are described as incoherent when no interference occurs, partially coherent when some interference occurs and coherent when a maximum amount of interference occurs, which is the case for two monochromatic waves of the same frequency.

Therefore, we would not expect any significant interference from two different light waves incident upon a soap film when the light waves are produced by a light source with a significant frequency bandwidth. However, there are two ways in which coherent light waves can be produced from a single light wave emitted by a light source with a significant frequency bandwidth: wavefront division and amplitude division.[38] In the case of a thin film, amplitude division occurs since the light wave is split into multiple wavefronts at the location of incidence of the light onto the upper surface of the film, as depicted in Fig. 2. If these coherent light waves later interfere, this process is known as interference by amplitude division. The waves leaving the upper surface of the film will only be partially coherent upon reaching a detector because there will be a time delay between the waves. Ultimately, finding the irradiance measured by a detector due to the interference of the light waves leaving the upper surface of the film in Fig. 2 will allow the variation of color with film thickness to be found.

E. The Fresnel equations

It is evident from Fig. 2 that light reflection and transmission occurs when light waves strike a thin film. In order to find the irradiance measured by a detector, it is necessary to consider how the amplitude of the electric field vector changes upon reflection and transmission of a light wave. The amplitude reflection and transmission coefficients, r and t, are defined by

$$r = \frac{E_{0\mathrm{r}}}{E_{0\mathrm{i}}}, \tag{8a}$$

$$t = \frac{E_{0\mathrm{t}}}{E_{0\mathrm{i}}}, \tag{8b}$$

where $E_{0\mathrm{i}}$ is the amplitude of the incident electric field vector (the electric field vector before reflection or transmission), and $E_{0\mathrm{r}}$ and

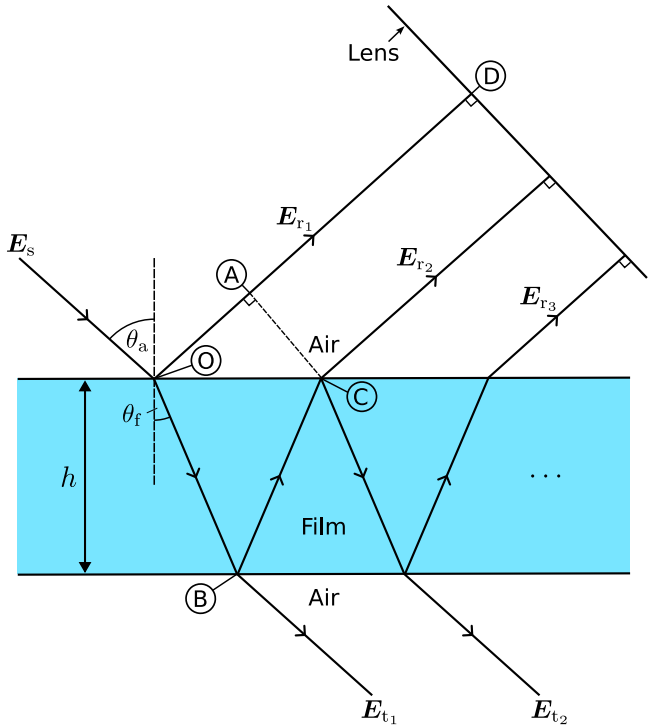

FIG. 2. Amplitude division in a very small section of thin film. Light rays are shown, which are perpendicular to the wavefronts of each wave and in the direction of wave propagation.

E_{0t} are the amplitudes of the reflected and transmitted electric field vectors, respectively. Considering the film in Fig. 2, which is surrounded by air on either side, the notation r and t will be used when the wave is in the air phase before reflection and transmission, and the notation r' and t' will be used when the wave is in the film phase before reflection and transmission.

For a wave incident onto a surface at a point, the plane of incidence is defined as the plane containing the incident wave vector $\boldsymbol{k}_s$ and the normal to the surface at the point of incidence. Light of any polarization may be expressed as the sum of two linearly polarized waves, where one of the waves has its electric field vector oriented parallel to the plane of incidence and the other has its electric field vector oriented perpendicular to the plane of incidence. Subscripts $\parallel$ and $\perp$ will be used to indicate when the electric field vector is parallel and perpendicular to the plane of incidence, respectively. Furthermore, a subscript $\bigstar$ will be used to indicate that an equation is valid for either case of polarization parallel or polarization perpendicular to the plane of incidence. The Fresnel equations, which are valid for light passing through linear, isotropic, and homogeneous media, provide expressions for the amplitude reflection and transmission coefficients. The Fresnel equations are given in Appendix B.

For a soap film created from water and bounded by air, the relative permeability of the air and film phases will be very close to 1. This allows the Fresnel equations to be simplified. The simplified Fresnel equations for the specific case of a soap film in air are also provided in Appendix B.

Reflectance R and transmittance T, which will allow the derived interference relations to be more compactly written, are defined by

$$R = \frac{P_r}{P_i}, \tag{9a}$$

$$T = \frac{P_t}{P_i}, \tag{9b}$$

where P_i is the radiant flux of the incident wave (the wave before reflection or transmission), and P_r and P_t are the radiant fluxes after reflection and transmission, respectively. A $'$ will also be added to R and T to indicate that the wave is in the film phase before reflection and transmission, rather than the air phase. Appendix C presents how the reflectance and transmittance can be expressed in term of the amplitude reflection and transmission coefficients. For a soap film in air,

$$R_\bigstar = (r_\bigstar)^2, \quad R'_\bigstar = (r'_\bigstar)^2, \tag{10a}$$

$$T_\bigstar = \frac{n_f \cos\theta_f}{n_a \cos\theta_a}(t_\bigstar)^2, \quad T'_\bigstar = \frac{n_a \cos\theta_a}{n_f \cos\theta_f}(t'_\bigstar)^2, \tag{10b}$$

where n_a and n_f are the absolute indices of refraction of the air and film phases, respectively, and θ_a and θ_f are the angles labeled in Fig. 2. From Eqs. (10) and (B2),

$$R_\bigstar = R'_\bigstar, \tag{11a}$$

$$T_\bigstar = T'_\bigstar = t_\bigstar t'_\bigstar, \tag{11b}$$

$$R_\bigstar + T_\bigstar = 1, \quad R'_\bigstar + T'_\bigstar = 1. \tag{11c}$$

Equation (11c) highlights how it is implicit in the Fresnel equations that no light absorbance is assumed.

Although reflection and transmission can lead to changes in light polarization,[40] any changes in polarization due to reflection and transmission will be neglected in this study.

F. Detector

Since the waves leaving the upper surface of the film in Fig. 2 are parallel for a very small section of film with uniform thickness, these waves will not interfere without the presence of a detector. In this work, a camera will be considered as the device that records the illuminated soap film. When light is collected by a modern camera, it first passes through a lens before hitting a digital sensor, which converts light into electrical signals. This digital sensor will serve as the detector in this work, where most modern cameras use either CCD or CMOS sensors. These sensors are split into millions of photosites, where the electrical signal produced by each photosite aligns with the light captured by that photosite. Multiple light waves leaving the upper surface of the film in Fig. 2 due to one incident light wave will strike a single photosite, and it is at the position of the photosite where light interference occurs. For example, each pixel in Fig. 1(b) covers a distance of 21.9 μm along the film. Using typical values for an illuminated soap film in air, as given in Table I of Appendix F, 49 waves leaving the upper film surface from a single incident wave would extend over a distance of 21.9 μm. Therefore, it would be possible for 49 waves, at most, to strike a single photosite from a single incident wave. The number of interfering waves in the context of interference calculations will be discussed in Sec. II H.

Each wave leaving the upper surface of the film in Fig. 2 travels a different distance from point O to the detector. Since each wave travels approximately the same distance from the camera lens to the detector, only the difference in distance traveled from point O to the camera lens needs to be considered in interference calculations, as will be done in Sec. II G.

G. Phase and time difference

When treating $\boldsymbol{E}_s$ as a monochromatic plane wave, an expression is needed for the difference in phase, δ, between each successive wave reaching the detector due to the difference in distance traveled from point O to the lens. In the case when the coherence between waves is accounted for, it is necessary to find the additional time, ξ, it takes for each successive wave to reach the detector from point O.

In this section, the difference in distance traveled by each light wave from point O to the lens due to the shape or angle of the lens

will be neglected, and the light waves will simply be assumed to be normally incident upon the lens.

For the jth wave reaching the lens from the upper surface of the film, the distance traveled from point O to the lens, d_j, is

$$d_j = (j-1)l_{\mathrm{OBC}} + (2-j)l_{\mathrm{OA}} + l_{\mathrm{AD}}, \quad j \in \mathbb{N}, \tag{12}$$

where l_{OBC}, l_{OA}, and l_{AD} are the distances covered by straight lines OBC, OA, and AD in Fig. 2, and $\mathbb{N}$ is the set of positive integers. For a monochromatic plane wave of wavelength λ_0, the change in phase $\Delta\phi_j$ (units: rad) due to the distance traveled from point O to the lens is

$$\Delta\phi_j = 2\pi\left(\frac{(j-1)l_{\mathrm{OBC}}}{\lambda_{\mathrm{f}}} + \frac{(2-j)l_{\mathrm{OA}} + l_{\mathrm{AD}}}{\lambda_0}\right), \quad j \in \mathbb{N}, \tag{13}$$

where λ_{f} is the wavelength of light in the film. It can be seen from Eq. (13) that the change in phase δ between each consecutive wave reaching the lens remains the same and may be written as

$$\delta = \Delta\phi_{j+1} - \Delta\phi_j = 2\pi\left(\frac{l_{\mathrm{OBC}}}{\lambda_{\mathrm{f}}} - \frac{l_{\mathrm{OA}}}{\lambda_0}\right), \quad j \in \mathbb{N}. \tag{14}$$

From Snell's law, $n_{\mathrm{a}}\sin\theta_{\mathrm{a}} = n_{\mathrm{f}}\sin\theta_{\mathrm{f}}$, and since $n_{\mathrm{f}}\lambda_f = n_{\mathrm{a}}\lambda_0$, Eq. (14) can be expressed as

$$\delta = \frac{4\pi h n_{\mathrm{f}}}{\lambda_0 n_{\mathrm{a}}}\cos\theta_{\mathrm{f}}, \tag{15}$$

where h is the film thickness. The shift in phase δ is due to the difference in distance traveled between each successive wave reaching the detector and does not account for phase changes due to reflection or transmission, which are accounted for by using the amplitude reflection and transmission coefficients. In deriving Eq. (15), it was assumed that the variation in thickness over the distance between each wave leaving the upper surface of the film, l_{OC}, is negligible. Using the values in Table I, $l_{\mathrm{OC}} = 445$ nm. In general, soap film thickness variations of the order of a hundred nanometers are expected over distances of the order of several millimeters, such as in Fig. 1(b); therefore, it is reasonable to consider the variation of thickness to be negligible over distances corresponding with several l_{OC}.

From Eq. (12), the time difference between successive waves reaching the detector from point O is

$$\xi = \frac{l_{\mathrm{OBC}}}{v_{\mathrm{f}}} - \frac{l_{\mathrm{OA}}}{v_{\mathrm{a}}}, \tag{16}$$

where v_{f} is the velocity of light in the film. Snell's law allows Eq. (16) to be simplified to

$$\xi = \frac{2hn_{\mathrm{f}}}{c}\cos\theta_{\mathrm{f}}, \tag{17}$$

where c is the speed of light in vacuum.

H. Interference of light at the detector without coherence effects

In this section, an interference equation for any number of interfering waves will be derived without accounting for the coherence between interfering waves. The electric field will be treated as a linearly polarized monochromatic plane wave when deriving this equation, with $\boldsymbol{E}_{\mathrm{s}}$ given by Eq. (6). For now, $\boldsymbol{E}_{\mathrm{s}}$ will be taken to be linearly polarized in the direction either parallel or perpendicular to the plane of incidence, and the ★ notation will be omitted for brevity. The ★ notation will be reintroduced once an equation has been derived for the detected irradiance, and it will then be highlighted how this equation can be used for light that is not simply linearly polarized in these directions, such as randomly polarized light. Following from Eq. (6), the electric field vector of the jth wave leaving the upper surface of the film is

$$\boldsymbol{E}_{\mathrm{r}j} = \boldsymbol{E}_{0\mathrm{r}j}\mathrm{e}^{\mathrm{i}(\boldsymbol{k}_{\mathrm{r}}\cdot\boldsymbol{r} + \epsilon_{\mathrm{r}} - \omega_0\tau + (j-1)\delta)}, \quad j \in \mathbb{N}, \tag{18}$$

where $\boldsymbol{k}_{\mathrm{r}}$ is the wave vector for waves leaving the upper surface of the film and ϵ_{r} is a phase constant. The phase constant ϵ_{r} is needed since $\boldsymbol{k}_{\mathrm{s}}\cdot\boldsymbol{r}$ and $\boldsymbol{k}_{\mathrm{r}}\cdot\boldsymbol{r}$ depend on the position of the origin. The value of ϵ_{r} can be found by noting that there is no change in phase upon reflection due to the position selected as the origin,[36]

$$\boldsymbol{k}_{\mathrm{s}}\cdot\boldsymbol{r} = \boldsymbol{k}_{\mathrm{r}}\cdot\boldsymbol{r} + \epsilon_{\mathrm{r}} \text{ at point O}. \tag{19}$$

From Eq. (7), the resultant electric field vector at the detector is

$$\boldsymbol{E}_{\mathrm{d}} = \sum_{j=1}^{N}\boldsymbol{E}_{\mathrm{r}j}, \tag{20}$$

where N is the number of waves that interfere at the detector due to the wave from the light source. At any time instant at the detector, $\boldsymbol{k}_{\mathrm{r}}\cdot\boldsymbol{r} + \epsilon_{\mathrm{r}} - \omega_0\tau$ is the same for each wave reaching the detector. Combining Eqs. (18) and (20) leads to

$$\boldsymbol{E}_{\mathrm{d}} = \mathrm{e}^{\mathrm{i}\chi}\sum_{j=1}^{N}\boldsymbol{E}_{0\mathrm{r}j}\mathrm{e}^{\mathrm{i}(j-1)\delta}, \tag{21}$$

where $\chi = \boldsymbol{k}_{\mathrm{r}}\cdot\boldsymbol{r} + \epsilon_{\mathrm{r}} - \omega_0\tau$. The amplitudes $E_{0\mathrm{r}j}$ may be written in terms of the amplitude reflection and transmission coefficients,

$$\begin{aligned} E_{0\mathrm{r}1} &= E_{0\mathrm{s}}r, \\ E_{0\mathrm{r}j} &= E_{0\mathrm{s}}t(r')^{2j-3}t', \quad j = 2, 3, \ldots, N. \end{aligned} \tag{22}$$

The first light wave leaving the upper surface of the film does not undergo any internal reflections within the film. This leads to a π rad phase shift between the first wave leaving the upper surface of the film and the rest of the waves leaving the upper surface of the film. This is embodied in Eq. (22) since r' is only present in odd powers and $r = -r'$. It is for this reason that very thin films appear black: for very thin films, the shift in phase δ will only be a small fraction of the wavelength, and assuming that the power in the first wave is similar to the total power in the other waves leaving the

upper film surface, the interference will be almost totally destructive. Inserting Eq. (22) into Eq. (21) and employing the relations in Eqs. (10) and (11) result in

$$\boldsymbol{E}_{\mathrm{d}} = \hat{\boldsymbol{E}}_{0\mathrm{r}} E_{0\mathrm{s}} \mathrm{e}^{\mathrm{i}\chi} \left[r + r' T \mathrm{e}^{\mathrm{i}\delta} \sum_{j=2}^{N} \left(R \mathrm{e}^{\mathrm{i}\delta} \right)^{j-2} \right], \tag{23}$$

where $\hat{\boldsymbol{E}}_{0\mathrm{r}}$ is the unit vector of the electric field for waves leaving the upper surface of the film, which is in the direction either parallel or perpendicular to the plane of incidence. The irradiance at the detector can be found from $\langle \boldsymbol{E}_{\mathrm{d}} \cdot \boldsymbol{E}_{\mathrm{d}}^{*} \rangle_T$,

$$I_{\mathrm{d}\bigstar} = I_{\mathrm{s}\bigstar} R_{\bigstar} \Bigg\{ 1 - 2T_{\bigstar} \sum_{j=2}^{N} R_{\bigstar}^{j-2} \cos(\delta(j-1)) + T_{\bigstar}^2 \sum_{j=2}^{N} \left(R_{\bigstar} \mathrm{e}^{-\mathrm{i}\delta} \right)^{j-2} \sum_{m=2}^{N} \left(R_{\bigstar} \mathrm{e}^{\mathrm{i}\delta} \right)^{m-2} \Bigg\}, \tag{24}$$

where $I_{\mathrm{s}\bigstar}$ is the irradiance of the light wave from the light source. From Eqs. (5) and (6), $I_{\mathrm{s}\bigstar} = \frac{1}{2} \epsilon_{\mathrm{a}} v_{\mathrm{a}} E_{0\mathrm{s}\bigstar}^2$. Appendix D shows how $I_{\mathrm{d}}/I_{\mathrm{s}}$ may be split into two parts, one due to interference and one not due to interference, to derive the following equation that is computationally easier to implement than Eq. (24):

$$I_{\mathrm{d}\bigstar} = I_{\mathrm{s}\bigstar} R_{\bigstar} \Bigg\{ 1 + T_{\bigstar}^2 \sum_{j=2}^{N} R_{\bigstar}^{2j-4} - 2T_{\bigstar} \sum_{j=2}^{N} R_{\bigstar}^{j-2} \cos(\delta(j-1)) + 2T_{\bigstar}^2 \sum_{j=2}^{N-1} R_{\bigstar}^{j-2} \sum_{m=j+1}^{N} R_{\bigstar}^{m-2} \cos(\delta(m-j)) \Bigg\}. \tag{25}$$

The first two terms on the right hand side of Eq. (25) represent the detected irradiance in the absence of interference. The last two terms in Eq. (25), the terms involving δ, are due to interference. Constructive interference occurs when the sum of these terms is positive, and destructive interference occurs when the sum is negative.

Equation (25) may be used to find the detected irradiance for light of any polarization by decomposing the light into the sum of electric field vectors that are oriented parallel and perpendicular to the plane of incidence. Then, $R_{\perp}$, $T_{\perp}$, and $I_{\mathrm{s}\perp}$ can be used in Eq. (25) to find $I_{\mathrm{d}\perp}$. Similarly, $R_{\parallel}$, $T_{\parallel}$, and $I_{\mathrm{s}\parallel}$ can be used in Eq. (25) to find $I_{\mathrm{d}\parallel}$. The overall value of I_{d} can then be computed by $I_{\mathrm{d}} = I_{\mathrm{d}\perp} + I_{\mathrm{d}\parallel}$. For randomly polarized light, such as light from the sun, $I_{\mathrm{s}\perp} = I_{\mathrm{s}\parallel} = \frac{1}{2} I_{\mathrm{s}}$.[36]

Using $N = 2$ in Eq. (25) leads to the interference equation given in Refs. 26, 30, 31, and 34. In order to analyze the choice of $N = 2$, the variation of $I_{\mathrm{d}}/I_{\mathrm{s}}$ with N was calculated using Eq. (25) for randomly polarized light and with the values given in Table I. The results are shown in Fig. 3 for three wavelengths of the incident wave from the source. The value of $I_{\mathrm{d}}/I_{\mathrm{s}}$ quickly converges to the value of $I_{\mathrm{d}}/I_{\mathrm{s}}$ at $N = \infty$ as N increases. This is due to the diminishing power in each additional wave leaving the upper surface of the film. Figure 3 suggests that, in this instance, $N = 5$ is an accurate number of waves to consider interfering since there will only be a small change in $I_{\mathrm{d}}/I_{\mathrm{s}}$ for increasing N beyond $N = 5$. In addition, it

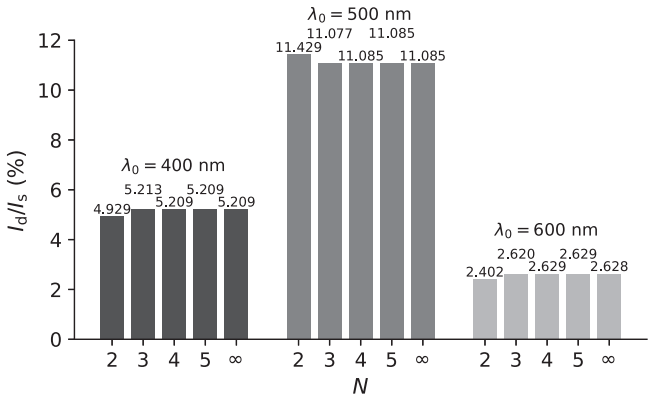

FIG. 3. The variation of $I_{\mathrm{d}}/I_{\mathrm{s}}$ with N for $h = 500\,\mathrm{nm}$ and $\lambda_0 \in \{400, 500, 600\}\,\mathrm{nm}$.

is reasonable to expect five light waves from a single incident light wave from the source to strike the same sensor photosite, as discussed in Sec. II F. Using $N = 2$, in this instance, provides a reasonable approximation to the result for $N = 5$ but does introduce some error. Furthermore, this error depends on the wavelength of the incident light wave and will increase as the reflectance increases. Therefore, we recommend that $N > 2$ is used in interference calculations as this will allow for a greater accuracy with only a slight increase in computational cost. Furthermore, although an infinite number of waves would not interfere in practice, the value of $I_{\mathrm{d}}/I_{\mathrm{s}}$ at $N = \infty$ could be used to approximate the true value of $I_{\mathrm{d}}/I_{\mathrm{s}}$. This is advantageous since an analytical equation can be derived for the detected irradiance for $N = \infty$, resulting in an increase in accuracy without an increase in computational cost.

For $N = \infty$, the Maclaurin series expansion of $\frac{1}{1-x}$,

$$\frac{1}{1-x} = \sum_{j=0}^{\infty} x^j, \; -1 < x < 1, \tag{26}$$

can be used in Eq. (23). The sum in Eq. (23) becomes

$$\sum_{j=2}^{\infty} \left(R \mathrm{e}^{\mathrm{i}\delta} \right)^{j-2} = \sum_{m=0}^{\infty} \left(R \mathrm{e}^{\mathrm{i}\delta} \right)^{m} = \frac{1}{1 - R\mathrm{e}^{\mathrm{i}\delta}}, \; R < 1, \tag{27}$$

which allows $\boldsymbol{E}_{\mathrm{d}}$ to be written as

$$\boldsymbol{E}_{\mathrm{d}} = \hat{\boldsymbol{E}}_{0\mathrm{r}} E_{0\mathrm{s}} \mathrm{e}^{\mathrm{i}\chi} \frac{r\left(1 - \mathrm{e}^{\mathrm{i}\delta}\right)}{1 - R\mathrm{e}^{\mathrm{i}\delta}}. \tag{28}$$

The irradiance measured by the detector can again be found from $\langle \boldsymbol{E}_{\mathrm{d}} \cdot \boldsymbol{E}_{\mathrm{d}}^{*} \rangle_T$. By making use of $\cos\delta = 1 - 2\sin^2\left(\frac{\delta}{2}\right)$, the detected

irradiance for $N = \infty$ is

$$I_{d\bigstar} = I_{s\bigstar}\frac{F_\bigstar \sin^2\left(\frac{\delta}{2}\right)}{1 + F_\bigstar \sin^2\left(\frac{\delta}{2}\right)}, \quad F_\bigstar = \frac{4R_\bigstar}{(1 - R_\bigstar)^2}. \tag{29}$$

Equation (29) is presented in Refs. 36 and 38.

The key limitation of using Eq. (25) to calculate interference colors for soap films illuminated by real light sources is that it predicts interference to occur for any film thickness, even very large film thicknesses. This is because Eq. (25) was derived using a monochromatic wave, which necessarily has an infinite coherence length and coherence time. However, the amount of interference is expected to decrease as the film thickness increases. This may be explained by considering the following: If the film thickness is small such that $\xi < \Delta t_c$ (the time between each wave reaching the detector is smaller than the coherence time of the light source), there will be a correlation between two adjacent waves reaching the detector since there will be a period of time at the detector where the two waves result from the same photon wavetrain in the light source. As a result, interference will occur. However, with a larger film thickness, ξ will be greater and the amount of correlation will fall as the overlap between non-correlated photon wavetrains at the detector will increase. In Sec. II I, we derive an interference relation that incorporates the necessary physics to predict the decrease in interference with increasing film thickness.

I. Interference of light at the detector including coherence effects

The aim of this section is to derive an equation for the irradiance at the detector that incorporates the degree of coherence between each pair of interfering waves. This will be done by considering the correlation between each wave reaching the detector. The electric field of the light from the source, $\boldsymbol{E}_s$, will no longer be governed by Eq. (6), but it will be assumed, for now, that $\boldsymbol{E}_s$ is linearly polarized in either the direction parallel or perpendicular to the plane of incidence. The ★ notation will be omitted for brevity and only reintroduced once the final equation for the detected irradiance has been derived.

Since each wave reaching the detector in amplitude division comes from the same original light wave, the correlation between each wave reaching the detector can be found through the self-coherence function, Γ, which is given by

$$\Gamma(\psi) = \langle \boldsymbol{E}_s(\tau + \psi) \cdot \boldsymbol{E}_s^*(\tau)\rangle_\Upsilon, \tag{30}$$

where ψ represents a time delay between the two waves. The field of $\boldsymbol{E}_s$ will be assumed to be stationary (any time averages are independent of the specific interval in time over which the averaging is performed), as is commonly the case in classical optics.[36,39] Consequently, Eq. (30) may be expressed as

$$\Gamma(\psi) = \lim_{\Upsilon\to\infty}\frac{1}{2\Upsilon}\int_{-\Upsilon}^{\Upsilon} \boldsymbol{E}_s(\tau + \psi) \cdot \boldsymbol{E}_s^*(\tau)\,d\tau. \tag{31}$$

Following from Eq. (31), the Fourier transform of the self-coherence function gives a power spectrum,[38,41]

$$\mathcal{F}\{\Gamma(\psi)\} = S(\omega), \tag{32}$$

where $\mathcal{F}$ is the Fourier transform and $S(\omega)$ is a power spectrum. The term $\frac{1}{2}\epsilon_a v_a S(\omega)$ has units of energy per unit area and describes the energy distribution of the light source.

The irradiance at the detector can be found from $\langle \boldsymbol{E}_d \cdot \boldsymbol{E}_d^*\rangle_\Upsilon$. Following from Eq. (20),

$$\langle \boldsymbol{E}_d \cdot \boldsymbol{E}_d^*\rangle_\Upsilon = \left\langle \sum_{j=1}^{N} \boldsymbol{E}_{rj} \cdot \sum_{m=1}^{N} \boldsymbol{E}_{rm}^* \right\rangle_\Upsilon, \tag{33}$$

which can be rewritten as the sum of non-interference and interference terms,

$$\langle \boldsymbol{E}_d \cdot \boldsymbol{E}_d^*\rangle_\Upsilon = \sum_{j=1}^{N}\langle \boldsymbol{E}_{rj} \cdot \boldsymbol{E}_{rj}^*\rangle_\Upsilon + 2\sum_{j=1}^{N-1}\sum_{m=j+1}^{N}\left\langle \Re\left\{\boldsymbol{E}_{rj} \cdot \boldsymbol{E}_{rm}^*\right\}\right\rangle_\Upsilon. \tag{34}$$

At any time instant at the detector, $\boldsymbol{E}_{rj}$ is a delayed version of $\boldsymbol{E}_{rm}$, but with a different amplitude, since $m > j$ in Eq. (34). The self-coherence function may be introduced into Eq. (34) since

$$\langle \boldsymbol{E}_{rj} \cdot \boldsymbol{E}_{rm}^*\rangle_\Upsilon = \frac{E_{0rj}}{E_{0s}}\frac{E_{0rm}}{E_{0s}}\Gamma((m - j)\xi). \tag{35}$$

Then, as shown in Appendix E, Eq. (34) becomes

$$\begin{aligned}\langle \boldsymbol{E}_d \cdot \boldsymbol{E}_d^*\rangle_\Upsilon = \Gamma(0)&\left(R + T^2\sum_{j=2}^{N} R^{2j-3}\right)\\ &- 2RT\sum_{m=2}^{N} R^{m-2}\Re\{\Gamma((m-1)\xi)\}\\ &+ 2RT^2\sum_{j=2}^{N-1} R^{j-2}\sum_{m=j+1}^{N} R^{m-2}\Re\{\Gamma((m-j)\xi)\}.\end{aligned} \tag{36}$$

It is useful to introduce a normalized self-coherence function, $\gamma(\psi)$, whose modulus satisfies $|\gamma(\psi)| \le 1$,

$$\gamma(\psi) = \frac{\Gamma(\psi)}{\Gamma(0)}. \tag{37}$$

Substituting $\gamma(\psi)\Gamma(0)$ in place of $\Gamma(\psi)$ in Eq. (36) and using $I_s = \frac{1}{2}\epsilon_a v_a \Gamma(0)$ leads to the final equation for the detected irradiance,

$$\begin{aligned}I_{d\bigstar} = I_{s\bigstar}R_\bigstar\Bigg\{&1 + T_\bigstar^2\sum_{j=2}^{N} R_\bigstar^{2j-4}\\ &- 2T_\bigstar\sum_{j=2}^{N} R_\bigstar^{j-2}\Re\{\gamma((j-1)\xi)\}\\ &+ 2T_\bigstar^2\sum_{j=2}^{N-1} R_\bigstar^{j-2}\sum_{m=j+1}^{N} R_\bigstar^{m-2}\Re\{\gamma((m-j)\xi)\}\Bigg\}.\end{aligned} \tag{38}$$

Equation (38) can be used for light polarized in an arbitrary direction or for randomly polarized light in the same way that Eq. (25) can, as detailed in Sec. II H.

When performing experiments on soap films, the spectral irradiance distribution of the light source is usually known rather than the time variation of the electric field of the light waves emitted by the source. Since $\Gamma(\psi) = \mathcal{F}^{-1}\{S(\omega)\}$, where $\mathcal{F}^{-1}$ is the inverse Fourier transform, $\gamma(\psi)$ can be found directly from $S(\omega)$,

$$\gamma(\psi) = \frac{\int_{-\infty}^{\infty} S(\omega) e^{i\omega\psi}\, d\omega}{\int_{-\infty}^{\infty} S(\omega)\, d\omega}. \tag{39}$$

It is expected that Eq. (38) becomes Eq. (25) in the limit of a monochromatic wave. For a monochromatic light wave given by Eq. (6), the self-coherence function can be found directly from Eq. (31), which leads to

$$\Gamma(\psi) = E_{0s}^2 e^{-i\omega_0\psi}. \tag{40}$$

From Eq. (40), $\gamma(\psi) = e^{-i\omega_0\psi}$ and $\Re\{\gamma((m-j)\xi)\}$ in Eq. (38) is $\cos(\omega_0(m-j)\xi)$. It can be shown through Eqs. (15) and (17) that $\omega_0\xi = \delta$. Therefore, for an incident monochromatic wave,

$$\Re\{\gamma((m-j)\xi)\} = \cos(\delta(m-j)), \tag{41}$$

from which it is clear that Eq. (38) becomes Eq. (25) for an incident monochromatic wave.

III. CONVERTING SPECTRAL IRRADIANCE DISTRIBUTIONS TO COLOR

The final step in finding the color of an illuminated soap film is to convert the spectral irradiance distribution at the detector to a color. In order to display the variation of color with film thickness on a standard computer monitor using the same primaries as the sRGB color space, the R, G, and B values need to be computed from the spectral irradiance distribution at the detector for each film thickness. This can be done by first calculating the X, Y, and Z values of the CIE XYZ color space for each film thickness. CIE color-matching functions allow for X, Y, and Z to be calculated from a given spectral irradiance distribution,[37]

$$X = \kappa \sum_{\lambda} I_\lambda(\lambda)\bar{x}(\lambda)\Delta\lambda, \tag{42a}$$

$$Y = \kappa \sum_{\lambda} I_\lambda(\lambda)\bar{y}(\lambda)\Delta\lambda, \tag{42b}$$

$$Z = \kappa \sum_{\lambda} I_\lambda(\lambda)\bar{z}(\lambda)\Delta\lambda, \tag{42c}$$

where κ is a constant, $\bar{x}$, $\bar{y}$, and $\bar{z}$ are color-matching functions, and $\Delta\lambda$ is the wavelength interval used in the summation. Where accuracy is desired, it is recommended that $\Delta\lambda = 1$ nm is used with a wavelength range from 360 to 830 nm.[37] This recommendation was used for all interference and color calculations performed in this study, which will be presented in Sec. IV. In addition, the CIE 1931 2 degree color-matching functions for a standard observer[42] were used for color computations.

The color components for any color space of interest can subsequently be found from the X, Y, and Z values calculated using Eq. (42). In order to convert to the sRGB color space, the X, Y, and Z values for all film thicknesses must be scaled by the same factor α so that the scaled values, given by $X_s = X/\alpha$, $Y_s = Y/\alpha$, and $Z_s = Z/\alpha$, are in the set [0, 1]. The chromaticity of a color is specified by its chromaticity coordinates, (x, y), which are defined by[37]

$$x = \frac{X}{X+Y+Z}, \tag{43a}$$

$$y = \frac{Y}{X+Y+Z}. \tag{43b}$$

Scaling X, Y, and Z by α keeps the chromaticity of the color constant but changes the luminance of the color, which is represented by Y. There is a free choice in what value α takes: there is a fixed range of brightnesses that the pixels in a computer screen can display, and a choice must be made of how the maximum brightness that can be displayed by a pixel relates to the calculated X, Y, and Z values. As a result, the absolute values of X, Y, and Z are unimportant when computing the color for display purposes; therefore, the absolute value of κ is not needed. Furthermore, a scaled version of $I_\lambda(\lambda)$ may be used in Eq. (42) since it is the relative values of X, Y, and Z that are of interest. Equations (25) and (38) both feature irradiance rather than spectral irradiance. Colors will be computed in Sec. IV by taking the relative spectral irradiance distribution at the detector to be a scaled version of the variation of irradiance with wavelength. There are a number of ways in which the scaling parameter α can be chosen. In the case that there is video footage featuring interference colors, we recommend that the value of the scaling factor is found by an optimization routine that minimizes the difference between the computed interference colors and the colors in the video.

Linear sRGB values, denoted by R^l, G^l, and B^l, can be found through matrix multiplication,[43]

$$\begin{pmatrix} R^l \\ G^l \\ B^l \end{pmatrix} = \begin{pmatrix} 3.2406 & -1.5372 & -0.4986 \\ -0.9689 & 1.8758 & 0.0415 \\ 0.0557 & -0.2040 & 1.0570 \end{pmatrix} \begin{pmatrix} X_s \\ Y_s \\ Z_s \end{pmatrix}. \tag{44}$$

The final sRGB values can be found by applying a gamma correction to the linear sRGB values,[43]

$$C = \begin{cases} -1.055(-C^l)^{\frac{1.0}{2.4}} + 0.055, & C^l < -V, \\ 12.92C^l, & |C^l| \le V, \\ 1.055(C^l)^{\frac{1.0}{2.4}} - 0.055, & C^l > V, \end{cases} \tag{45}$$

where C is a corrected R, G, or B value, C^l is the respective linear value, and $V = 0.003\,130\,8$. Some of the computed R, G, or B values may be out of the range [0, 1] since the gamut of the sRGB colorspace covers only around 35% of the XYZ colorspace.[44] Therefore, any colors that lie outside of the color gamut of a monitor with the same primaries as the sRGB colorspace must be

converted to colors that can be represented by the monitor. A number of methods exist for mapping out-of-gamut colors into the colorspace,[30] such as finding the color with the least perceivable difference that can be represented by the monitor. In this work, the simplest approach of clipping any R, G, or B values outside of the set [0, 1] to 0 or 1 was adopted. This is equivalent to clipping the R^t, G^t, and B^t values outside of the set [0, 1] to 0 or 1 and then applying the gamma correction. The color-science Python package[45] was used for color-specific calculations performed in this work.

IV. INTERFERENCE AND COLOR CALCULATIONS

Interference calculations were performed to find the variation of color with film thickness for light sources of different frequency bandwidths. Coherence effects were accounted for in Sec. IV A by using Eq. (38). In contrast, interference calculations were performed in Sec. IV B by using Eq. (25), which does not account for coherence effects. The values given in Table I of Appendix F were used for the calculations in Secs. IV A and IV B, and it was assumed that the light source emitted randomly polarized light.

A. Calculations incorporating coherence effects

This section details the use of Eq. (38) to find interference colors for light sources of different frequency bandwidths.

Each photosite on a camera sensor records a single irradiance value, regardless of the range of frequencies in the light that is incident upon the photosite. Similarly, Eq. (38) results in a single value for the detected irradiance for light containing a range of frequencies. Color cannot be extracted from a single irradiance value. It is for this reason that a color filter array is used in cameras.[46] The most widely used color filter array is the Bayer matrix or Bayer mosaic, which involves placing one of three color filters in front of each photosite. Color is then extracted by comparing the brightness values recorded by a photosite and its neighboring photosites in a process known as demosaicing. To allow for an analytical treatment while approximately replicating the demosaicing process used in a camera, the spectral irradiance distribution of the light source was taken to be composed of three individual Gaussian distributions, where each Gaussian distribution corresponds to the light source being passed through a different color filter. The power spectrum $S(\omega)$ of each Gaussian spectral irradiance distribution is also Gaussian since the power spectrum is a scaled version of the spectral irradiance distribution. We are able to perform this scaling since only relative values are needed for the color computations, as outlined in Sec. III.

For the jth Gaussian spectrum, $j \in \{1, 2, 3\}$,

$$S_j(\omega) = \frac{A_j}{\sigma\sqrt{2\pi}}\left(e^{-\frac{1}{2}\frac{(\omega-\overline{\omega}_j)^2}{\sigma^2}} + e^{-\frac{1}{2}\frac{(\omega+\overline{\omega}_j)^2}{\sigma^2}}\right), \tag{46}$$

where A_j and $\overline{\omega}_j$ are the amplitude and mean angular frequency of the jth Gaussian spectrum, respectively, and σ is a parameter controlling the frequency bandwidth of the source. The observable spectrum is represented by the positive frequencies in $S_j(\omega)$ and the three Gaussian spectra were centered at wavelengths 460, 550, and 610 nm.

Both $\Gamma(0)$ and γ are needed to use Eq. (38). For the jth Gaussian spectrum,

$$\Gamma_j(\psi) = \frac{A_j}{\pi}\cos(\overline{\omega}_j\psi)e^{-\frac{1}{2}\sigma^2\psi^2}, \tag{47a}$$

$$\gamma_j(\psi) = \cos(\overline{\omega}_j\psi)e^{-\frac{1}{2}\sigma^2\psi^2}, \tag{47b}$$

as shown in Appendix G 1. At each film thickness, the value of ξ was computed using Eq. (17) and I_d was found from $I_{d\perp} + I_{d\parallel}$ for each of the three Gaussian spectra by using Eq. (47) in Eq. (38) with $N = 5$. To avoid the complexity of the demosaicing process, the spectral irradiance distribution at the detector was assumed to follow three Gaussian distributions with the same value of σ and the same value of $\overline{\omega}_j$ as in the source but where the amplitude was determined by the calculated value of I_d. This approach, which is illustrated in Fig. 4, leads to differences in the computed colors compared with the colors that would be recorded by a camera, but we favor this approach here to keep the analysis analytical. Figure 4(a) presents the relative source spectrum for $\sigma = 0.06\overline{\omega}_2$, and Fig. 4(b) shows the relative spectral irradiance distribution at the detector for $h = 500$ nm and the source in Fig. 4(a). The value of A_j for each Gaussian spectrum was chosen so that the chromaticity of the light source (from the sum of the three Gaussian distributions) matched the chromaticity of the D65 illuminant, given by $(x, y) = (0.3127, 0.3290)$ for the CIE 1931 2 degree color-matching functions,[37] for each value of σ investigated. The relative amplitudes of each Gaussian spectrum are provided in Table II in Appendix G 2.

The detected spectral irradiance distribution for each film thickness was then converted to a color using the method detailed in Sec. III. This was done for five sources of different frequency bandwidths (five different values of σ), and the resulting thickness–color relationships are presented in Fig. 5. The same scaling factor α was used for each of the five sources investigated to allow for a comparison between the thickness–color relationships and was chosen so that the maximum Z_s value for $\sigma = 0.06\overline{\omega}_2$ was 0.8.

The color at each film thickness in Fig. 5 depends on the amplitude of each of the three Gaussian distributions in the detected spectral irradiance distribution. For example, the blue at around $h = 250$ nm results from the first Gaussian distribution, centered at $\overline{\lambda}_1 = 460$ nm, dominating the detected spectral irradiance distribution.

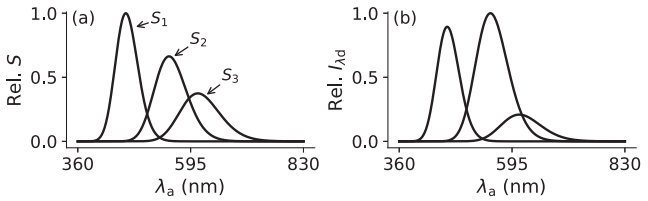

FIG. 4. (a) Visible part of the relative power spectrum for $\sigma = 0.06\overline{\omega}_2$ and (b) the relative spectral irradiance distribution at the detector for $h = 500$ nm, where λ_a is the wavelength in air.

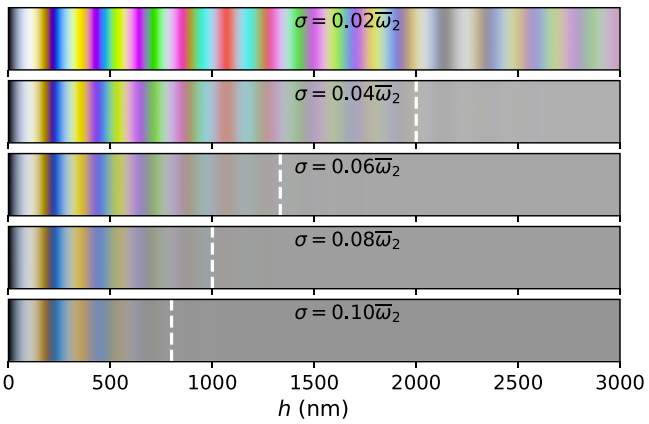

FIG. 5. Variation of color with film thickness for $\sigma \in [0.02, 0.10]\overline{\omega}_2$. The dashed white lines mark h_c from Eq. (49).

As the film thickness increases, particularly for larger values of σ, the colored fringes in Fig. 5 fade. This occurs because an increase in the film thickness results in a decrease in the coherence between any pair of waves at the detector, as is accounted for by Eq. (38).

Although no sharp transition in the amount of interference is expected to occur when the time between successive waves reaching the detector is equal to the coherence time ($\xi = \Delta t_c$), particularly given that multiple definitions exist for the coherence time of a source,[39] it is expected that the amount of interference occurring is small when $\xi = \Delta t_c$. The coherence time is frequently taken to be the full width half maximum of the modulus of $\gamma(\psi)$.[41,47] Using this definition, the coherence time for each Gaussian spectrum may be expressed in terms of σ as

$$\Delta t_c = \frac{2\sqrt{2\ln 2}}{\sigma}. \tag{48}$$

Inserting Eq. (48) into Eq. (17) and rearranging for the film thickness leads to

$$h_c = \frac{c\sqrt{2\ln 2}}{n_f \cos\theta_f \sigma}, \tag{49}$$

where h_c is the film thickness when $\xi = \Delta t_c$. White dashed lines on Fig. 5 mark h_c. It is evident from the grayish color that only a small amount of interference is taking place for $h > h_c$. This is quantified in Fig. 6(a), which shows the variation of I_d/I_s with film thickness for each of the three Gaussian power spectra for $\sigma = 0.10\overline{\omega}_2$. As h increases beyond h_c, I_d/I_s converges toward

$$\frac{1}{2}R_\perp\left(1 + T_\perp^2\sum_{j=2}^{N}R_\perp^{2j-4}\right) + \frac{1}{2}R_\parallel\left(1 + T_\parallel^2\sum_{j=2}^{N}R_\parallel^{2j-4}\right)$$

since the interference terms in Eq. (38) tend to 0. Similarly, as h increases beyond h_c, the chromaticity coordinates tend toward those of the D65 illuminant, as shown in Fig. 6(b).

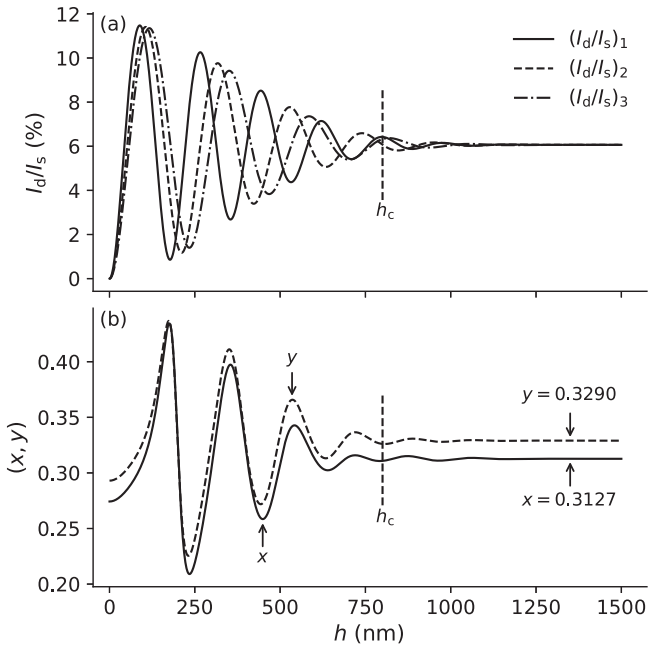

FIG. 6. The variation of (a) I_d/I_s and (b) chromaticity with film thickness for $\sigma = 0.10\overline{\omega}_2$.

B. Calculations without coherence effects

In this section, interference colors are calculated by applying Eq. (25) at a discrete number of wavelengths in the light source, in alignment with the method detailed in Refs. 29–33. This method relies on the assumption stated in Sec. II B.

To allow for a comparison with the colors calculated in Sec. IV A, the light source was modeled as the sum of the three Gaussian distributions that were used in Sec. IV A for each value of σ. This is shown in Fig. 7(a) for $\sigma = 0.06\overline{\omega}_2$.

In order to use Eq. (25) at a discrete number of wavelengths in the source, the source spectral irradiance distribution must split into intervals of wavelength of width $\Delta\lambda$. The irradiance I_s in an interval centered on λ_0 can be approximated by $I_{\lambda s}(\lambda_0)\Delta\lambda$, as discussed in Sec. II A. In this work, $\Delta\lambda = 1$ nm was used with $\lambda_0 = 360, 361, \ldots, 830$ nm. This leads to 471 values of I_s, where it

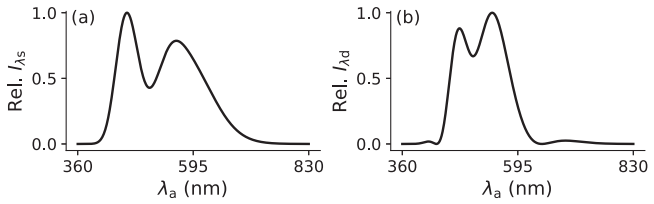

FIG. 7. Relative spectral irradiance distribution of (a) the source for $\sigma = 0.06\overline{\omega}_2$ and (b) at the detector for $h = 500$ nm.

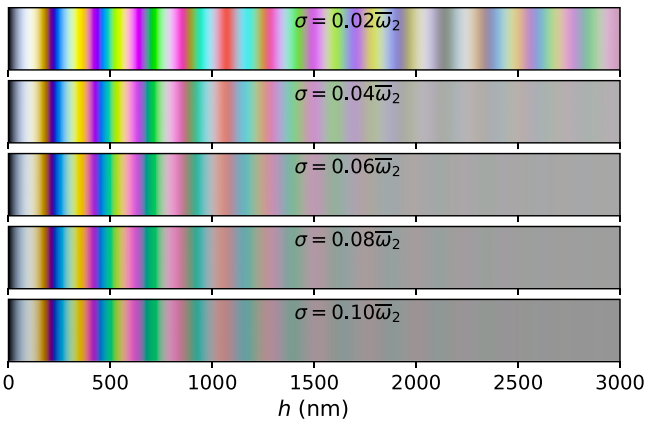

FIG. 8. Variation of color with film thickness for $\sigma \in [0.02, 0.10]\overline{\omega}_2$.

is assumed that each of these I_s values comes from a monochromatic plane wave oscillating at a frequency corresponding with λ_0. At each film thickness, Eq. (25) was used for each of the 471 monochromatic waves with $N = 5$. This allows the relative spectral irradiance distribution at the detector to be found for each film thickness. The relative spectral irradiance distribution at the detector for $h = 500$ nm and for the source in Fig. 7(a) is shown in Fig. 7(b).

The color was then calculated for each film thickness using the method outlined in Sec. III with the same value of the scaling factor α that was used in Sec. IV A. The resulting thickness–color relationships are shown in Fig. 8.

The colors fade to a color which has the same chromaticity as the light source as the film thickness increases. It is tempting to think that this is because the coherence between any pair of waves at the detector falls as the film thickness increases. Although this is true, the effects of coherence are not captured by Eq. (25). The reason the colors fade to a color that has the same chromaticity as the light source may be explained by considering how δ varies with a change in the wavelength, $\Delta\lambda$. From Eq. (15), the change in δ, $\Delta\delta$, when λ changes from λ_0 to $\lambda_0 + \Delta\lambda$ is

$$\Delta\delta = \frac{4\pi h n_f \cos\theta_f}{n_a} \frac{\Delta\lambda}{\lambda_0(\lambda_0 + \Delta\lambda)}. \tag{50}$$

From Eq. (50), the range of wavelengths $\Delta\lambda$ between adjacent monochromatic waves undergoing total constructive interference at a given film thickness decreases as the film thickness increases.

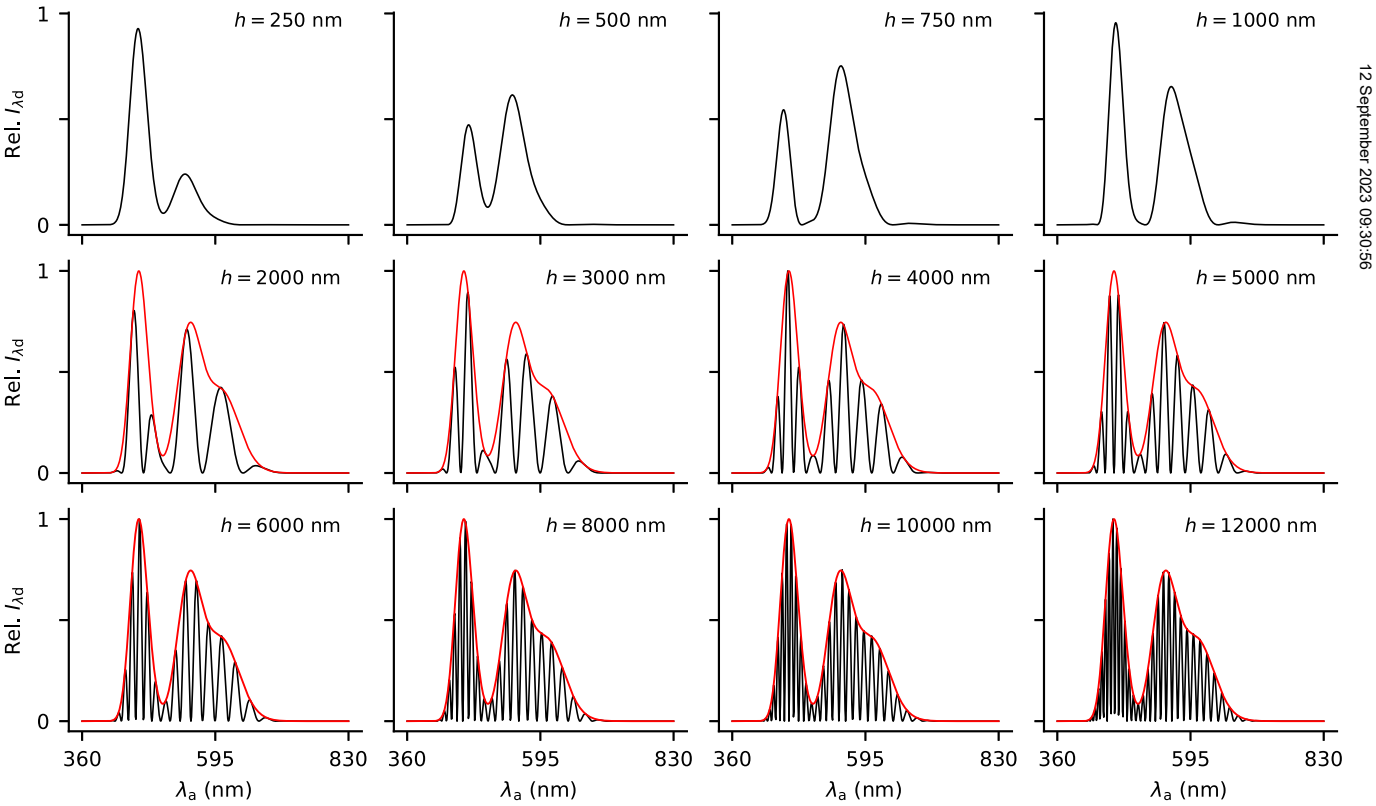

FIG. 9. Relative spectral irradiance distributions at the detector for $\sigma = 0.04\overline{\omega}_2$ and $h \in [250, 12\,000]$ nm. The scaling was chosen so that the maximum $I_{\lambda d}$ is 1 for $h = 12\,000$ nm. $I_{\lambda s}$ scaled to a maximum of 1 is overlaid in red onto the spectral irradiance distributions for $h \geq 2000$ nm.

Consequently, the number of interference maxima over the range of wavelengths in the visible spectrum increases as the film thickness increases, which leads to the detected spectral irradiance distribution to more closely resemble the source spectral irradiance distribution. This is illustrated in Fig. 9. For example, for small film thicknesses, such as $h = 250\,\text{nm}$ and $h = 500\,\text{nm}$, there are only one or two interference maxima in the detected spectral irradiance distribution. This results in a vibrant color at those film thicknesses in Fig. 8. With increasing film thickness in Fig. 9, the number of interference minima and maxima increases. At interference minima, I_d is close to 0 and the contribution to X, Y, and Z, given by Eq. (42), will be small. At an interference maximum, the value of $I_{\lambda\text{d}}$ depends on the value of $I_{\lambda\text{s}}$ at that wavelength. A scaled version of the source spectral irradiance distribution has been plotted in Fig. 9, from which it is clear that the interference maxima in the detected spectral irradiance distribution increasingly well replicate the distribution of the light source for increasing film thickness beyond around $h = 3000\,\text{nm}$. It is for this reason that the computed interference fringes shown in Fig. 8 fade with increasing film thickness. The oscillations of $I_{\lambda\text{d}}$ in Fig. 9 with varying wavelength indicate that interference is still occurring for film thicknesses as large as 12 μm. These oscillations will continue to occur as the film thickness is ever increased since each light wave is being regarded as monochromatic.

For reference, a code implementing the method of using Eq. (25) at a discrete number of wavelengths in the source to calculate interference colors is available in Ref. 48.

V. DISCUSSION

This section compares the colors calculated in Secs. IV A and IV B with the aim of understanding when interference relations derived for monochromatic waves can faithfully be applied to find interference colors.

A comparison between Figs. 5 and 8 for $\sigma = 0.02\overline{\omega}_2$ highlights that the colors calculated are largely similar when the frequency bandwidth of the light source is small. However, with increasing frequency bandwidth, the colors are more vibrant at smaller film thicknesses and fade slower at larger film thicknesses in Fig. 8 compared with Fig. 5.

A quantitative comparison between the colors in Figs. 5 and 8 without the effect of luminance can be performed by comparing the variation of chromaticity with film thickness. This is useful since the luminance is affected by the scaling factor α, while the chromaticity is not. A comparison of the computed chromaticities for $\sigma = 0.04\overline{\omega}_2$ and $\sigma = 0.08\overline{\omega}_2$ is presented in Fig. 10, where (x_c, y_c) are the chromaticity coordinates of the colors from Sec. IV A and (x_m, y_m) are the chromaticity coordinates of the colors from Sec. IV B.

For $\sigma = 0.04\overline{\omega}_2$, the variation of chromaticity with film thickness is very similar for thicknesses below 650 nm. However, the peaks of both x and y are higher, and the troughs in x and y are lower when using the method detailed in Sec. IV B. This highlights how the reduction in coherence between any pair of waves at the detector with increasing film thickness has the effect of damping the chromaticity coordinates. This is particularly evident in Figs. 10(c) and 10(d), which shows that there is a greater damping of the chromaticity coordinates when the bandwidth of the source is greater. This means that in any thickness interval featuring interference colors, a wider range of colors is present in Fig. 8 compared with Fig. 5.

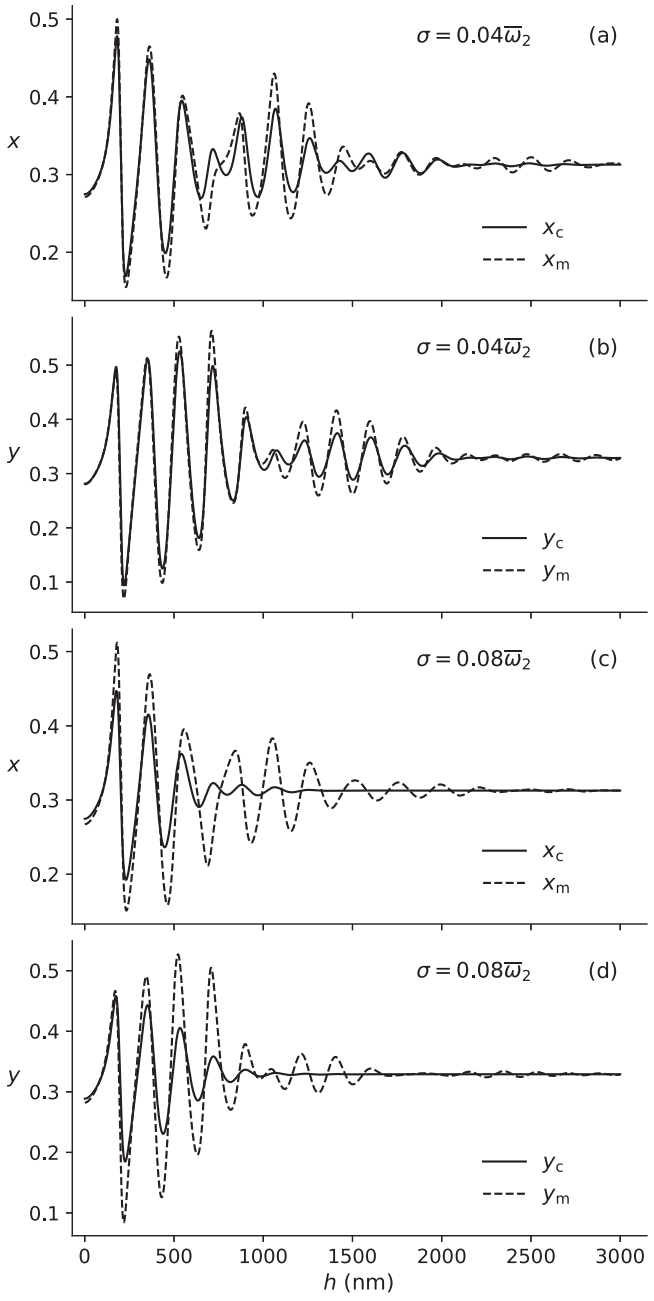

FIG. 10. The variation of chromaticity with film thickness for $\sigma = 0.04\overline{\omega}_2$ and $\sigma = 0.08\overline{\omega}_2$.

At each film thickness, the difference in color, ϕ, between the colors calculated in Secs. IV A and IV B can be quantified by

the Euclidean distance between the colors in the chromaticity space,

$$\phi = \sqrt{(x_m - x_c)^2 + (y_m - y_c)^2}. \quad (51)$$

A moving average of ϕ is presented in Fig. 11 for the five light sources investigated in this work. For small film thicknesses (where the colors have not faded to the chromaticity of the light source), Fig. 11 illustrates that the color differences are greater when the frequency bandwidth of the light source is greater.

Taking (x_c, y_c) to be the chromaticity coordinates of the true color, ϕ serves as a measure of the error caused by using the method detailed in Sec. IV B. By defining an allowable value for the color difference, which we will denote as ϕ_a, a threshold thickness can be defined for each source beyond which the method detailed in Sec. IV B should not be used for color calculations. For example, for $\phi_a = 0.06$, Fig. 11 suggests that the method of Sec. IV B may be used faithfully for all film thicknesses when $\sigma = 0.02\overline{\omega}_2$ and $\sigma = 0.04\overline{\omega}_2$. On the other hand, the threshold thickness is 415 nm for $\sigma = 0.06\overline{\omega}_2$ and this value decreases with increasing frequency bandwidth of the source. For example, the threshold thickness becomes 166 nm for $\sigma = 0.10\overline{\omega}_2$. The threshold thickness depends on the spectral irradiance distribution of the light source; therefore, the analysis to find the thickness below which Eq. (25) can accurately calculate interference colors must be conducted for each light source of interest. Furthermore, the method that a camera uses to extract colors from irradiance measurements should be used to allow for a more accurate analysis of when Eq. (25) can be applied to find interference colors. Therefore, a key part of future work will be to use Eq. (38) to account for the coherence between waves with the precise method that a camera uses to produce a colored image. This will involve filtering the light leaving one of the film surfaces with each of the color filters used by a camera. Equation (38) will then be applied to calculate the irradiance measured by each photosite covered by each color filter; this will involve finding the required self-coherence functions computationally through the inverse discrete Fourier transform. Subsequently, a demosaicing algorithm will be implemented to find the three-channel RGB color data for each pixel in the image. This will provide a very general method for calculating the interference colors exhibited by a soap film while accounting for coherence effects.

Additional points worth considering when performing interference and color calculations for soap films are provided in Appendix H.

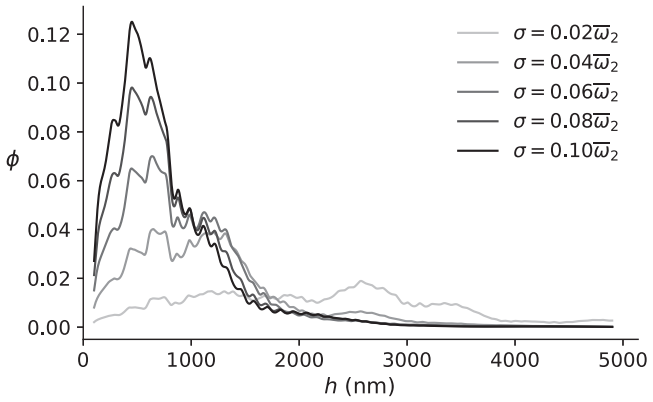

FIG. 11. Color differences calculated using Eq. (51) for $\sigma \in [0.02, 0.10]\overline{\omega}_2$. The lines shown are moving averages over 200 nm of thickness. Each average is shown at the center of the thickness interval used for averaging.

VI. CONCLUSIONS

This study introduces an interference relation for soap films that accounts for the expected decrease in coherence between interfering waves with increasing film thickness and sheds light on the range of applicability of an interference relation derived for monochromatic waves. Our findings suggest that the thickness below which the relation derived for monochromatic waves can be used to accurately calculate interference colors decreases with increasing frequency bandwidth of the source. For the light sources investigated in the present study, there is a close agreement between the colors calculated using the relation accounting for coherence and the relation derived for monochromatic waves over the entire range of film thicknesses typical of a soap film when the frequency bandwidth of each of the Gaussian distributions comprising the light source is smaller than 29 THz ($\sigma = 0.02\overline{\omega}_2$). With larger frequency bandwidths, coherence effects start to become important at typical soap film thicknesses. For example, when each Gaussian distribution has a frequency bandwidth of 87 THz ($\sigma = 0.06\overline{\omega}_2$), the relation derived for monochromatic waves only shows good accuracy up to film thicknesses of the order of half a micrometer. Overall, the introduced interference relation that accounts for the coherence between interfering waves will enable the thickness of soap films to be more accurately found from interference colors.

ACKNOWLEDGMENTS

This work was supported by the Engineering and Physical Sciences Research Council (Grant No. EP/T51780X/1).

AUTHOR DECLARATIONS

Conflict of Interest

The authors have no conflicts to disclose.

Author Contributions

Navraj S. Lalli: Conceptualization (lead); Formal analysis (lead); Investigation (lead); Methodology (lead); Writing – original draft (lead); Writing – review & editing (equal). **Andrea Giusti:** Supervision (lead); Writing – review & editing (equal).

DATA AVAILABILITY

The data that support the findings of this study are available within the article.

APPENDIX A: IRRADIANCE FROM THE COMPLEX REPRESENTATION OF AN ELECTRIC FIELD

We are interested in writing $\langle \tilde{E}^2 \rangle_\Upsilon$, the time average of the magnitude of the electric field squared over a time period Υ at a given point in space, in terms of the complex representation of the electric field, $\boldsymbol{E}$, so that the irradiance can be found from the complex representation. We will consider $\boldsymbol{E}$ in its most general form: $\boldsymbol{E} = \boldsymbol{E}_0(\tau)e^{i\phi(\tau)}$, where we are computing the time average at a fixed point in space so that the variation in $\boldsymbol{E}$ with position need not be considered. The time average of the magnitude of the electric field squared is

$$\langle \tilde{E}^2 \rangle_\Upsilon = \langle \tilde{\boldsymbol{E}} \cdot \tilde{\boldsymbol{E}} \rangle_\Upsilon. \tag{A1}$$

Since $\tilde{\boldsymbol{E}} = \frac{1}{2}(\boldsymbol{E} + \boldsymbol{E}^*)$,

$$\tilde{\boldsymbol{E}} \cdot \tilde{\boldsymbol{E}} = \frac{1}{4}(2\boldsymbol{E} \cdot \boldsymbol{E}^* + \boldsymbol{E} \cdot \boldsymbol{E} + \boldsymbol{E}^* \cdot \boldsymbol{E}^*). \tag{A2}$$

From Eqs. (A1) and (A2),

$$\langle \tilde{E}^2 \rangle_\Upsilon = \frac{1}{2}\langle \boldsymbol{E} \cdot \boldsymbol{E}^* \rangle_\Upsilon + \frac{1}{2}\langle \Re\{\boldsymbol{E} \cdot \boldsymbol{E}\} \rangle_\Upsilon. \tag{A3}$$

The phase term will disappear in $\boldsymbol{E} \cdot \boldsymbol{E}^*$; therefore, the time average involving this term will be non-zero. On the other hand, $\Re\{\boldsymbol{E} \cdot \boldsymbol{E}\} = E_0^2(\tau)\cos 2\phi(\tau)$. The phase of the electric field at a fixed point in space will vary in time such that the time average of $\Re\{\boldsymbol{E} \cdot \boldsymbol{E}\}$ over a period of time much greater than the time period of a typical oscillation will be 0. Consequently, Eq. (A3) simplifies to

$$\langle \tilde{E}^2 \rangle_\Upsilon = \frac{1}{2}\langle \boldsymbol{E} \cdot \boldsymbol{E}^* \rangle_\Upsilon, \tag{A4}$$

which allows for the irradiance to be found using the complex representation.

APPENDIX B: THE FRESNEL EQUATIONS FOR A SOAP FILM IN AIR

For light passing through linear, isotropic, and homogeneous media, the Fresnel equations are[36]

$$r_\perp = \frac{E_{0r\perp}}{E_{0i\perp}} = \frac{\frac{n_i}{\mu_i}\cos\theta_i - \frac{n_t}{\mu_t}\cos\theta_t}{\frac{n_i}{\mu_i}\cos\theta_i + \frac{n_t}{\mu_t}\cos\theta_t}, \tag{B1a}$$

$$t_\perp = \frac{E_{0t\perp}}{E_{0i\perp}} = \frac{2\frac{n_i}{\mu_i}\cos\theta_i}{\frac{n_i}{\mu_i}\cos\theta_i + \frac{n_t}{\mu_t}\cos\theta_t}, \tag{B1b}$$

$$r_\parallel = \frac{E_{0r\parallel}}{E_{0i\parallel}} = \frac{\frac{n_t}{\mu_t}\cos\theta_i - \frac{n_i}{\mu_i}\cos\theta_t}{\frac{n_i}{\mu_i}\cos\theta_t + \frac{n_t}{\mu_t}\cos\theta_i}, \tag{B1c}$$

$$t_\parallel = \frac{E_{0t\parallel}}{E_{0i\parallel}} = \frac{2\frac{n_i}{\mu_i}\cos\theta_i}{\frac{n_i}{\mu_i}\cos\theta_t + \frac{n_t}{\mu_t}\cos\theta_i}, \tag{B1d}$$

where n_j, μ_j, and θ_j are the absolute indices of refraction, permeabilities, and angles labeled in Fig. 12. Subscripts i, r, and t represent "incident," "reflected," and "transmitted," respectively.

For a soap film in air, the Fresnel equations in Eq. (B1) simplify to

$$r_\perp = \frac{n_a\cos\theta_a - n_f\cos\theta_f}{n_a\cos\theta_a + n_f\cos\theta_f}, \tag{B2a}$$

$$r'_\perp = \frac{n_f\cos\theta_f - n_a\cos\theta_a}{n_f\cos\theta_f + n_a\cos\theta_a}, \tag{B2b}$$

$$t_\perp = \frac{2n_a\cos\theta_a}{n_a\cos\theta_a + n_f\cos\theta_f}, \tag{B2c}$$

$$t'_\perp = \frac{2n_f\cos\theta_f}{n_f\cos\theta_f + n_a\cos\theta_a}, \tag{B2d}$$

$$r_\parallel = \frac{n_f\cos\theta_a - n_a\cos\theta_f}{n_a\cos\theta_f + n_f\cos\theta_a}, \tag{B2e}$$

$$r'_\parallel = \frac{n_a\cos\theta_f - n_f\cos\theta_a}{n_f\cos\theta_a + n_a\cos\theta_f}, \tag{B2f}$$

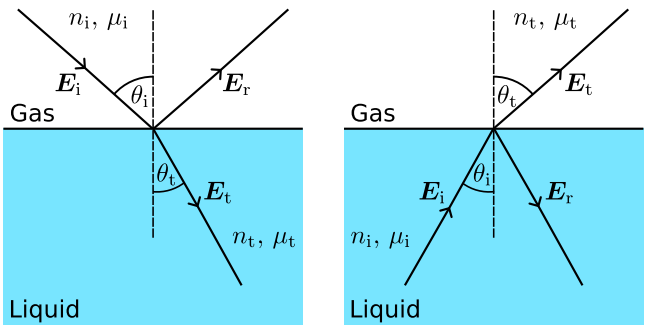

FIG. 12. Reflection at and transmission through a gas–liquid interface: the initial wave is in the gas phase on the left and in the liquid phase on the right.

$$t_{\parallel} = \frac{2n_a \cos\theta_a}{n_a \cos\theta_f + n_f \cos\theta_a}, \tag{B2g}$$

$$t'_{\parallel} = \frac{2n_f \cos\theta_f}{n_f \cos\theta_a + n_a \cos\theta_f}, \tag{B2h}$$

where subscripts a and f denote the air and film phases, respectively. By using the Fresnel equations in this study, we are assuming that the air and the soap film are linear, homogeneous, and isotropic dielectrics.

APPENDIX C: REFLECTANCE AND TRANSMITTANCE

In terms of irradiances, the reflectance and transmittance are given by[36]

$$R_\star = \frac{I_{r\star}}{I_{i\star}}, \tag{C1a}$$

$$T_\star = \frac{I_{t\star}\cos\theta_t}{I_{i\star}\cos\theta_i}, \tag{C1b}$$

where $\star$ is either $\perp$ or $\parallel$, and I_i, I_r, and I_t are the incident, reflected, and transmitted irradiances, respectively. Note that $I_i = I_{i\perp} + I_{i\parallel}$, $I_r = I_{r\perp} + I_{r\parallel}$, and $I_t = I_{t\perp} + I_{t\parallel}$. Equation (2) allows $R_\star$ and $T_\star$ to be written in terms of the amplitude reflection and transmission coefficients,[36]

$$R_\star = (r_\star)^2, \tag{C2a}$$

$$T_\star = \frac{n_t \cos\theta_t}{n_i \cos\theta_i}(t_\star)^2. \tag{C2b}$$

The derivation of Eq. (C2b) assumes $\mu_t = \mu_i$. This is used with $v_t^2 = \frac{1}{\mu_t \epsilon_t}$ and $v_i^2 = \frac{1}{\mu_i \epsilon_i}$ to simplify $\frac{\epsilon_t v_t}{\epsilon_i v_i}$ to $\frac{v_i}{v_t}$.

APPENDIX D: INTERFERENCE AT THE DETECTOR WITHOUT COHERENCE EFFECTS

In order to derive Eq. (25) from Eq. (24), part of the last term in Eq. (24),

$$L = \sum_{j=2}^{N} \left(Re^{-i\delta}\right)^{j-2} \sum_{m=2}^{N} \left(Re^{i\delta}\right)^{m-2}, \tag{D1}$$

can be expressed as the sum of terms that are not due to interference and the sum of terms that are due to interference,

$$L = \sum_{j=2}^{N} R^{2j-4} + \sum_{j=2}^{N-1}\sum_{m=j+1}^{N} \left[\left(Re^{i\delta}\right)^{m-2}\left(Re^{-i\delta}\right)^{j-2} + \left(Re^{i\delta}\right)^{j-2}\left(Re^{-i\delta}\right)^{m-2}\right]. \tag{D2}$$

Since $\left(Re^{i\delta}\right)^{m-2}\left(Re^{-i\delta}\right)^{j-2} + \left(Re^{i\delta}\right)^{j-2}\left(Re^{-i\delta}\right)^{m-2} = 2R^{m-2}R^{j-2}\cos(\delta(m-j))$, Eq. (D2) can be simplified to

$$L = \sum_{j=2}^{N} R^{2j-4} + 2\sum_{j=2}^{N-1} R^{j-2} \sum_{m=j+1}^{N} R^{m-2}\cos(\delta(m-j)). \tag{D3}$$

Equation (25) is obtained by inserting Eq. (D3) into Eq. (24).

APPENDIX E: INTERFERENCE AT THE DETECTOR WITH COHERENCE EFFECTS

This section shows how Eq. (36) can be obtained from Eq. (34). Using Eq. (35) in Eq. (34) results in

$$\langle \boldsymbol{E}_d \cdot \boldsymbol{E}_d^* \rangle_\Gamma = \Gamma(0)\sum_{j=1}^{N}\left(\frac{E_{0rj}}{E_{0s}}\right)^2 + 2\sum_{j=1}^{N-1}\frac{E_{0rj}}{E_{0s}}\sum_{m=j+1}^{N}\frac{E_{0rm}}{E_{0s}}\Re\{\Gamma((m-j)\xi)\}. \tag{E1}$$

Equation (22) suggests that the $j = 1$ terms in Eq. (E1) should be evaluated separately, which leads to

$$\langle \boldsymbol{E}_d \cdot \boldsymbol{E}_d^* \rangle_\Gamma = \Gamma(0)\left(r^2 + \sum_{j=2}^{N}\left(\frac{E_{0rj}}{E_{0s}}\right)^2\right) + 2r\sum_{m=2}^{N}\frac{E_{0rm}}{E_{0s}}\Re\{\Gamma((m-1)\xi)\} + 2\sum_{j=2}^{N-1}\frac{E_{0rj}}{E_{0s}}\sum_{m=j+1}^{N}\frac{E_{0rm}}{E_{0s}}\Re\{\Gamma((m-j)\xi)\}. \tag{E2}$$

Equation (22) allows for E_{0rj}/E_{0s} and E_{0rm}/E_{0s} in Eq. (E2) to be evaluated. By also invoking the relations in Eqs. (10) and (11), Eq. (E2) takes the form

$$\langle \boldsymbol{E}_d \cdot \boldsymbol{E}_d^* \rangle_\Gamma = \Gamma(0)\left(R + T^2\sum_{j=2}^{N} R^{2j-3}\right) + 2rT\sum_{m=2}^{N}(r')^{2m-3}\Re\{\Gamma((m-1)\xi)\} + 2T^2\sum_{j=2}^{N-1}(r')^{2j-3}\sum_{m=j+1}^{N}(r')^{2m-3}\Re\{\Gamma((m-j)\xi)\}, \tag{E3}$$

which can be written as Eq. (36) by again using Eqs. (10) and (11).

APPENDIX F: TYPICAL VALUES FOR A SOAP FILM IN AIR

Typical values for n_a, n_f, h, and θ_a for an illuminated soap film in air are given in Table I. Amplitude reflection and transmission coefficients, which were calculated from n_a, n_f, and θ_a through

TABLE I. Typical values for an illuminated soap film in air. The values for n_a, n_f, h, and θ_a were prescribed, while the values for the reflectance, transmittance, and amplitude coefficients were calculated.

n_a	n_f	h	θ_a
1.00	1.41[34]	500 nm	35°
$r_\perp$	$r'_\perp$	$t_\perp$	$t'_\perp$
−0.2225	0.2225	0.7775	1.2225
$R_\perp$	$R'_\perp$	$T_\perp$	$T'_\perp$
0.049 52	0.049 52	0.9505	0.9505
$r_\parallel$	$r'_\parallel$	$t_\parallel$	$t'_\parallel$
0.1167	−0.1167	0.7920	1.2454
$R_\parallel$	$R'_\parallel$	$T_\parallel$	$T'_\parallel$
0.013 63	0.013 63	0.9864	0.9864

Snell's law and Eq. (B2), and reflectance and transmittance values, which were calculated using Eq. (10), are provided in Table I. The variation of the absolute indices of refraction of the air and the soap film with the wavelength of light has not been accounted for here.

APPENDIX G: CALCULATIONS WITH COHERENCE EFFECTS

1. Self-coherence function of a Gaussian spectrum

The self-coherence function in Eq. (47) can be derived by first considering the Gaussian power spectrum $S'(\omega)$ centered at $\omega = 0$,

$$S'(\omega) = \frac{A}{\sigma\sqrt{2\pi}} e^{-\frac{1}{2}\frac{\omega^2}{\sigma^2}}. \tag{G1}$$

The self-coherence function of $S'(\omega)$ will be denoted by $\Gamma'(\psi)$. From Eq. (32),

$$\Gamma'(\psi) = \frac{1}{2\pi}\frac{A}{\sigma\sqrt{2\pi}}\int_{-\infty}^{\infty} e^{-\frac{1}{2}\frac{\omega^2}{\sigma^2}} e^{i\omega\psi}\, d\omega. \tag{G2}$$

By completing the square,

$$-\frac{1}{2}\frac{\omega^2}{\sigma^2} + i\omega\psi = -\frac{1}{2\sigma^2}(\omega - \sigma^2 i\psi)^2 - \frac{1}{2}\sigma^2\psi^2, \tag{G3}$$

which can be inserted into Eq. (G2), leading to

$$\Gamma'(\psi) = \frac{1}{2\pi}\frac{A}{\sigma\sqrt{2\pi}} e^{-\frac{\sigma^2\psi^2}{2}}\int_{-\infty}^{\infty} e^{-\frac{1}{2\sigma^2}(\omega-\sigma^2 i\psi)^2}\, d\omega. \tag{G4}$$

Upon making the substitution $u = \omega - \sigma^2 i\psi$, Eq. (G4) becomes

$$\Gamma'(\psi) = \frac{1}{2\pi}\frac{A}{\sigma\sqrt{2\pi}} e^{-\frac{\sigma^2\psi^2}{2}}\int_{-\infty-\sigma^2 i\psi}^{\infty-\sigma^2 i\psi} e^{-\frac{u^2}{2\sigma^2}}\, du. \tag{G5}$$

Using Cauchy's integral theorem, it can be shown that the integral in Eq. (G5) evaluates to $\sigma\sqrt{2\pi}$ and the final equation for $\Gamma'(\psi)$ is

$$\Gamma'(\psi) = \frac{A}{2\pi} e^{-\frac{1}{2}\sigma^2\psi^2}. \tag{G6}$$

We are interested in the power spectrum $S(\omega) = S'(\omega - \overline{\omega}) + S'(\omega + \overline{\omega})$ with self-coherence function $\Gamma(\psi)$. Therefore, $\Gamma(\psi) = \mathcal{F}^{-1}\{S'(\omega - \overline{\omega})\} + \mathcal{F}^{-1}\{S'(\omega + \overline{\omega})\}$, where

$$\mathcal{F}^{-1}\{S'(\omega - \overline{\omega})\} = e^{i\overline{\omega}\psi}\Gamma'(\psi), \tag{G7a}$$

$$\mathcal{F}^{-1}\{S'(\omega + \overline{\omega})\} = e^{-i\overline{\omega}\psi}\Gamma'(\psi). \tag{G7b}$$

Consequently,

$$\begin{aligned}\Gamma(\psi) &= \Gamma'(\psi)\left[e^{i\overline{\omega}\psi} + e^{-i\overline{\omega}\psi}\right] \\ &= \frac{A}{\pi}\cos(\overline{\omega}\psi)e^{-\frac{1}{2}\sigma^2\psi^2},\end{aligned} \tag{G8}$$

which aligns with Eq. (47).

2. Amplitudes of the Gaussian power spectra

The relative amplitudes of the Gaussian power spectra used in Sec. IV A were found by fixing the amplitude of the Gaussian spectrum centered at $\overline{\lambda}_1 = 460$ nm and varying the amplitudes of the other two Gaussian spectra so that the resulting chromaticity of a light source comprised of the sum of the three Gaussian spectra was the same as the chromaticity of the D65 illuminant.

APPENDIX H: ADDITIONAL CONSIDERATIONS

When the interference phenomena on the opposite side of the soap film are of interest, the interference relation for light waves leaving the lower film surface can be derived by noting that the detected irradiance on each side of the film will sum to equal the incident irradiance, assuming the absorbance of light by the film can be neglected.

The interference relations derived as part of this work assume that the soap film is surrounded by the same gas on each side of the film. The derivation should be modified when the media on each side of the soap film have different absolute indices of refraction since the reflectance and transmittance inside the film would no longer be the same at the upper and lower film interfaces.

Real light sources extend over space. Therefore, light will strike a point on a soap film over a range of angles. However, only

TABLE II. Relative amplitudes of the Gaussian power spectra used in Sec. IV A.

σ	A_1	A_2	A_3
$0.02\overline{\omega}_2$	1.0000	0.7712	0.3835
$0.04\overline{\omega}_2$	1.0000	0.7263	0.3725
$0.06\overline{\omega}_2$	1.0000	0.6635	0.3745
$0.08\overline{\omega}_2$	1.0000	0.5479	0.4289
$0.10\overline{\omega}_2$	1.0000	0.3741	0.5285

some of the resulting light waves leaving the film surface will reach a detector. By modeling the light source as a number of independent point sources, the overall interference pattern may be found by summing the interference pattern due to each point source.[38]

REFERENCES

[1]V. Bergeron, "Forces and structure in thin liquid soap films," J. Phys.: Condens. Matter **11**, R215 (1999).
[2]Y. Couder, J. Chomaz, and M. Rabaud, "On the hydrodynamics of soap films," Physica D **37**, 384 (1989).
[3]Y. Couder, "Two-dimensional grid turbulence in a thin liquid film," J. Phys. Lett. **45**, 353 (1984).
[4]H. Kellay and W. I. Goldburg, "Two-dimensional turbulence: A review of some recent experiments," Rep. Prog. Phys. **65**, 845 (2002).
[5]T. Meuel, Y. L. Xiong, P. Fischer, C.-H. Bruneau, M. Bessafi, and H. Kellay, "Intensity of vortices: From soap bubbles to hurricanes," Sci. Rep. **3**, 3455 (2013).
[6]L.-J. Yang, C. Tasupalli, R. Waikhom, and N. Panchal, "Soap film visualization of a 10 cm-span flapping wing," Fluids **6**, 361 (2021).
[7]M. Gharib and P. Derango, "A liquid film (soap film) tunnel to study two-dimensional laminar and turbulent shear flows," Physica D **37**, 406 (1989).
[8]M. Fayed, R. Portaro, A.-L. Gunter, H. A. Abderrahmane, and H. D. Ng, "Visualization of flow patterns past various objects in two-dimensional flow using soap film," Phys. Fluids **23**, 091104 (2011).
[9]S. Poulain, E. Villermaux, and L. Bourouiba, "Ageing and burst of surface bubbles," J. Fluid Mech. **851**, 636 (2018).
[10]A. Gros, A. Bussonnière, S. Nath, and I. Cantat, "Marginal regeneration in a horizontal film: Instability growth law in the nonlinear regime," Phys. Rev. Fluids **6**, 024004 (2021).
[11]J. Miguet, M. Pasquet, F. Rouyer, Y. Fang, and E. Rio, "Marginal regeneration-induced drainage of surface bubbles," Phys. Rev. Fluids **6**, L101601 (2021).
[12]R. V. Craster and O. K. Matar, "Dynamics and stability of thin liquid films," Rev. Mod. Phys. **81**, 1131 (2009).
[13]N. S. Lalli, L. Shen, D. Dini, and A. Giusti, "The stability of magnetic soap films," Phys. Fluids **35**, 057116 (2023).
[14]T. Galy, M. Marszewski, S. King, Y. Yan, S. H. Tolbert, and L. Pilon, "Comparing methods for measuring thickness, refractive index, and porosity of mesoporous thin films," Microporous Mesoporous Mater. **291**, 109677 (2020).
[15]B. Wang, B. Ke, B. Chen, R. Li, and R. Tian, "A technical review of research progress on thin liquid film thickness measurement," Exp. Comput. Multiph. Flow **2**, 199 (2020).
[16]V. Greco, C. Lemmi, S. Ledesma, G. Molesini, G. Puccioni, and F. Quercioli, "Measuring soap black films by phase shifting interferometry," Meas. Sci. Technol. **5**, 900 (1994).
[17]M. Vannoni, A. Sordini, R. Gabrieli, M. Melozzi, and G. Molesini, "Measuring the thickness of soap bubbles with phase-shift interferometry," Opt. Express **21**, 19657 (2013).
[18]S.-W. Kim and G.-H. Kim, "Thickness-profile measurement of transparent thin-film layers by white-light scanning interferometry," Appl. Opt. **38**, 5968 (1999).
[19]O. Krichevsky and J. Stavans, "Surfactant-polymer interactions in soap films," Physica A **200**, 743 (1993).
[20]F. Bouchama and J.-M. Di Meglio, "Rheological studies of freely suspended soap films," Colloid Polym. Sci. **278**, 195 (2000).
[21]S. Berg, E. A. Adelizzi, and S. M. Troian, "Experimental study of entrainment and drainage flows in microscale soap films," Langmuir **21**, 3867 (2005).
[22]J. Miguet, M. Pasquet, F. Rouyer, Y. Fang, and E. Rio, "Stability of big surface bubbles: Impact of evaporation and bubble size," Soft Matter **16**, 1082 (2020).
[23]X. Wu, R. Levine, M. Rutgers, H. Kellay, and W. Goldburg, "Infrared technique for measuring thickness of a flowing soap film," Rev. Sci. Instrum. **72**, 2467 (2001).
[24]P. D. Huibers and D. O. Shah, "Multispectral determination of soap film thickness," Langmuir **13**, 5995 (1997).
[25]V. Prasad and E. R. Weeks, "Flow fields in soap films: Relating viscosity and film thickness," Phys. Rev. E **80**, 026309 (2009).
[26]A. S. C. Lawrence, *Soap Films: A Study of Molecular Individuality* (G. Bell, 1929).
[27]M. L. Dias, "Ray tracing interference color," IEEE Comput. Graph. Appl. **11**, 54 (1991).
[28]M. L. Dias, "Ray tracing interference color: Visualizing Newton's rings," IEEE Comput. Graph. Appl. **14**, 17 (1994).
[29]C. Isenberg, "The science of soap films and soap bubbles" (Tieto Ltd., 1978).
[30]B. E. Smits and G. W. Meyer, "Newton's colors: Simulating interference phenomena in realistic image synthesis," in *Photorealism in Computer Graphics* (Springer, 1992), pp. 185–194.
[31]A. Glassner, "Soap bubbles: Part 2," IEEE Comput. Graph. Appl. **20**, 99 (2000).
[32]D. Jaszkowski and J. Rzeszut, "Interference colours of soap bubbles," Vis. Comput. **19**, 252 (2003).
[33]W. Huang, J. Iseringhausen, T. Kneiphof, Z. Qu, C. Jiang, and M. B. Hullin, "Chemomechanical simulation of soap film flow on spherical bubbles," ACM Trans. Graph. **39**, 41 (2020).
[34]D. Lovett, *Demonstrating Science With Soap Films* (IOP Publishing, 1994).
[35]M. Kness, "Colorpy: A python package for handling physical descriptions of color and light spectra." The source package can be found at https://github.com/markkness/ColorPy (2008).
[36]E. Hecht, *Optics* (Pearson Education India, 2012).
[37]C. T. Committee, "Colorimetry," Technical Report, 3rd ed. (International Commission on Illumination, 2004).
[38]M. Bass, *Handbook of Optics: Volume I-Geometrical and Physical Optics, Polarized Light, Components and Instruments* (McGraw-Hill Education, 2010).
[39]L. Mandel and E. Wolf, *Optical Coherence and Quantum Optics* (Cambridge University Press, 1995).
[40]D. H. Goldstein, *Polarized Light*, 3rd ed. (CRC press, 2017).
[41]W. Drexler and J. G. Fujimoto, *Optical Coherence Tomography: Technology and Applications* (Springer Science & Business Media, 2008).
[42]International Commission on Illumination, CIE 1931 colour-matching functions, 2 degree observer (data table), Vienna, Austria (2018).
[43]International Electrotechnical Commission *et al.*, IEC 61966-2-1 International Standard, multimedia systems and equipment–colour measurement and management, part 2.1: default RGB colour space–sRGB, Amendment , 1 (2003).
[44]H. Le, T. Jeong, A. Abdelhamed, H. J. Shin, and M. S. Brown, "Gamutnet: Restoring wide-gamut colors for camera-captured images," in *Color and Imaging Conference*, 29 (Society for Imaging Science and Technology, 2021), pp. 7–12.
[45]T. Mansencal, M. Mauderer, M. Parsons, N. Shaw, K. Wheatley, S. Cooper *et al.* (2022). "Colour 0.4.2," Zenodo. https://doi.org/10.5281/zenodo.7367239.
[46]I. Pekkucuksen and Y. Altunbasak, "Multiscale gradients-based color filter array interpolation," IEEE Trans. Image Process. **22**, 157 (2012).
[47]C. Akcay, P. Parrein, and J. P. Rolland, "Estimation of longitudinal resolution in optical coherence imaging," Appl. Opt. **41**, 5256 (2002).
[48]N. S. Lalli (2023). "Colour-soap-films v1.0.0," Zenodo. https://doi.org/Zenodo doi:10.5281/zenodo.7658215.